

Research on the quality, mineralogical and structural conditions of silico-ferrite of calcium and aluminum (SFCA) phases in iron ore sinter

Ömer Saltuk Bölükbaşı (✉ osaltuk.bolukbasi@iste.edu.tr)

Iskenderun Technical University

Research Article

Keywords: Sinter, mineralogy, phase composition, image analysis, Rietveld, SFCA

Posted Date: May 26th, 2022

DOI: <https://doi.org/10.21203/rs.3.rs-1668551/v1>

License: © ⓘ This work is licensed under a Creative Commons Attribution 4.0 International License.

[Read Full License](#)

Abstract

Silico-ferrite of calcium and aluminum (SFCA), a significant equilibrium crystalline phase in the Fe_2O_3 - CaO - Al_2O_3 - SiO_2 ternary structure, is an effective bonding form in the sintering process of fine iron ore. The current study investigates the effects of using pellet dust instead of iron ore in sinter blend in SFCA phases. Investigation of the internal structure of the sinter is critical in terms of its physical and metallurgical properties. In this study, the sinter pot experimental conditions were simulated to the actual sinter mill situation. The chemical structure of SFCA compounds was defined as both SFCA and SFCA-I phases in the SiO_2 - CaO - Fe_2O_3 and Si-Ca-Fe ternary-phase system. The comparison of the sinter samples with each other revealed that the sinter mixture with a pellet dust fraction of 13.53% in the Sin-3 probably achieved the best similarity in reaction rate and formed the larger ratios in SFCA and SFCA-I. In addition, this research optimized the chemical composition in the sintering process (especially CaO , Al_2O_3 , Fe_2O_3 , SiO_2 , etc.), investigated the correlation between the SFCA phases (SFCA and SFCA-I), and controlled the main parameters that affect on the sintering process and its functioning.

Introduction

Sinter mineralogy and macro and microstructure are directly related to sinter quality and strength. The mineral structure of the sintered material depends on the sinter composition. Therefore, it is necessary to realize the basic requirements of the phase structure throughout the sintering process to control and improve the sintering property. The reaction in the sintering process and the phase structures have been the subject of many studies (Hsieh 1989; Scarlett et al. 2004). During the sintering process, chemical reactions occur at high temperatures (about 1200 °C). The iron ores and flux materials are mixed to form a sinter cake of iron ore, silicoferrites of calcium and aluminum (SFCA), larnite, and a glassy structure. SFCA is the most significant component of the formation due to its abundance in the sintered material and its considerable effect on sintering. Many studies have particularly examined the accumulation and structure of the SFCA structure formed during the sintering process (Lv 2011; Yang et al. 1997). Besides, many scientists have investigated SFCA phase structures and recognized the inadequacy of available phase forms for SFCA structures (Yang et al. 1997). Many reactions occurred during the sintering process can cause the existence of different compounds in the sintered material (Loo 1998).

SFCA structures are the most favored forming structure in sinter due to their extreme reducibility, excellent mechanical strength, and low degradation, which are significant parameters in determining the efficiency and capacity of the blast furnaces (Wei et al. 2018; Loo 1998; Webster et al. 2012). Understanding the formation of the various stages in the sintering process will provide higher product quality, production optimization, and economic savings. For this purpose, numerous research has been carried out with X-ray diffraction and the Rietveld method. Significant forms of the calcium ferrite phases with different morphologies are generally gathered under the SFCA title, depending on the conditions under which the sintered structure occurs. The first SFCA type appears in a blocky or columnar form during the cooling phase when the sintering temperature is at 1300°C (Webster et al. 2016; Koryttseva et al. 2017; Cai et al. 2018; Nicol et al. 2018). Many researchers have reported that the crystal grain size of SFCA formation can

be over 10 μm in this phase (Sasaki and Hida 1982; Garbers-Craig et al, 2003). SFCA morphology has $\text{M}_{14}\text{O}_{20}$ stoichiometry, a chemical formula of $\text{Ca}^{+2}_{2.3}\text{Mg}^{+2}_{0.8}\text{Al}^{+3}_{1.5}\text{Fe}^{+3}_{8.3}\text{Si}^{+4}_{1.1}\text{O}^{-2}_{20}$ and a low-Fe-high-silica and alumina composition (Cai et al. 2018; Nicol et al.2018; Nyembwe et al. 2015).

The second type of SFCA (SFCA-I), occurs between 1200 and 1300°C and might be in platy, acicular, or needle-like shaped morphology (Loo et al.1998; Cai et al. 2018, Sasaki and Hida 1982; Van Den Berg and De Villiers 2009). Reportedly, this growth in the crystal structure ranges from 4 μm to 10 μm (Garbers-Craig et al. 2003; Dawson et al. 1984). SFCA-I has $\text{M}_{20}\text{O}_{28}$ stoichiometry and its chemical formula is $\text{Ca}^{+2}_{3.18}\text{Fe}^{+3}_{15.48}\text{Al}^{+3}_{1.34}\text{O}^{-2}_{28}$. It has high Fe_2O_3 and low Al and Si composition (Webster et al. 2016; Cai et al, 2018, Nicol et al, 2018). Although both SFCA and SFCA-I phase structures contain Fe^{+2} and Fe^{+3} , the SFCA-I phase structure has more Fe^{+2} (Mumme et al. 1998; Webster et al. 2017). The highest replacement ratio in SFCA was confirmed to be between Fe^{+3} and Al^{+3} (Webster et al. 2016; Koryttseva et al. 2017; Kalenga and Garbers 2008). Only Fe_2O_3 is observed in the SFCA phase, but FeO and Fe_3O_4 are not (Dawson et al. 1984; Das et al. 2001). A limited number of studies have been carried out on creating a stable SFCA-I phase structure in the sinter matrix. The SFCA-I phase structure begins to form at 1050°C in the first stage of sintering, and when the sintering temperature exceeds $\sim 1220\text{--}1240^\circ\text{C}$, it undergoes fractures, and the product in the sinter is replaced by SFCA and hematite (Kalenga and Garbers 2008; Scarlett et al. 2004; Fernández-González 2017). Hida and Sasaki (1983) and Pownceby et al. (2003) reported that the SFCA-I structure provides high strength, quality, and reducibility in a sintered material.

The third type of SFCA, SFCA-II, is the first SFCA phase structure type formed during the sintering process (Mumme et al. 2003; Villiers and Verryn 2008; Fernández-González 2018). SFCA-II is a thin dendritic (triple bond structure) morphological form, and it is formed at a sintering temperature of about 700°C during the sintering process. Dawson et al. (1983) and Garbers-Craig et al. (2003) reported that the dendritic crystals constituting the morphological structure of SFCA II are thin and generally smaller than 4 μm . Mumme (2003), Lister and Glasser (1967) researched SFCA-II. SFCA-II is a significant phase in the $\text{Fe}_2\text{O}_3\text{-CaO-Al}_2\text{O}_3$ ternary system between 973K and 1723K (between 700°C to 1450°C). SFCA II has an $\text{M}_{34}\text{O}_{48}$ stoichiometry, and its chemical formula is $\text{Ca}^{+2}_{5.1}\text{Al}^{+3}_{9.3}\text{Fe}^{+3}_{18.7}\text{Fe}^{+2}_{0.9}\text{O}^{-2}_{48}$. According to Mumme (Hamilton et al. 1989), it appears to be a composition or intermediate structure between SFCA and SFCA-I crystal structures. Recently, Van Den Berg and JPR De Villiers (2009), Van Den Berg (2008) have reported that SFCA-II is available in sinter plants in South Africa. The effect of the SFCA-II phase's structure and sinter matrix on quality, chemical properties, hot-cold strength, and control parameters has been little studied. Hsieh has announced that acicular SFCA, a great sinter bonding structure, makes the sinter stronger and reducible with its microporous structure. As the sintered structure acts as an adhesive for the sintered matrix, SFCA-I plays a critical role in achieving sinter quality (Hsieh and Ja 1989). The enhanced sensitivity of the phase forming mechanisms of SFCA and SFCA-I in the sintered material can provide improved performance in the industrial sintering process. The SFCA phase in the sintering process substantially contributes to improving the metallurgical properties and quality parameters such as the Tumbler Index (TI), Reduction Degradation Index (RDI), and metallurgical properties (Hida et al. 1983;

Honeyands 2019; Mitra and Nath 2005). Pellet material is an efficient charge material fed to the blast furnace. Up to 6% of the pellet material turns into pellet dust during production and transportation. Pellet dust is added to the sinter mix in the dosing unit. It is usually sieved before being fed to the blast furnace.

The current study, using the pellet dust in the sinter blend instead of fine iron ore, examined the effect of pellet dust on the physical and metallurgical properties of the sinter. In order to complete the SEM and XRD analysis, the study examined the detailed view of the mineralogical compounds, their elemental composition, and elements' valence conditions by applying the EDS method. The study investigated phase structures of hematite, magnetite, larnite, SFCA, SFCA-I, and wuestite using an optical microscope according to melting and temperature. In addition, the phase structure types of SFCA, SFCA-I, and SFCA-II in the sinter matrix were investigated by applying pellet dust at different rates. The results were interpreted with the Rietveld Method.

Materials And Methods

Materials used in experimental studies were main iron ore, Iron ore (A), Iron ore (A) pellet dust, Flue dust, mill scale, iron-containing waste material (i.e., return sinter dust, Basic Oxygen Furnace (BOF) slag), coke breeze and fluxes. In the study, samples of the raw materials used in the sintered test study were taken and prepared for the "sinter pot test" study. The sinter pot test was designed according to the requirements of industrial sinter plant conditions. Test studies were conducted to determine the effect of the pellet dust on the sinter compositions (especially on the SFCA phases) and the sintered product's quality. For experimental analysis, five sinter samples were prepared and named Sin-1, Sin-2, Sin-3, Sin-4, and Sin-5. Laboratory studies were carried out in a laboratory sinter vessel with a diameter of 250 mm and a height of 450 mm. Table 1 shows the sintering test conditions.

Table 1
Sintering test conditions.

Suction at fan	1050 mmWG
Return fines in the sinter mix	23%
Sintering Time: 25 min.	25 min.
CaO/SiO ₂ ratio of the sinter	1.90
MgO in sinter	1.3%
Heat input for ignition	1050 °C
Bed height	550 mm
Coke breeze consumption	70 kg/t ⁻¹ of sinter
Moisture :7.0%	7.0%
Limestone 5.50%	5.50%
Dolomite 2.30%	2.30%
Coke breeze (-3 mm)	> 88%
Limestone and dolomite (-3 mm)	> 90%

Figure 1 shows the laboratory sinter pot apparatus used in the tests. Five experimental groups were set up to investigate the efficiencies of the phase structures in sinter samples and to evaluate the results obtained from various pellet dusts in sinter mixtures. Samples were prepared by mixing different amounts of pellet dust for the experiments (Table 2). Usage rates of pellet dust were determined as 0.00%, 9.11%, 13.53%, 17.88%, and 21.86% by mass in the sinter blend. Sinter pot test conditions were simulated with actual sinter plant conditions in process and operation. The sintering process and operating conditions were kept the same for all tests. Fine particle pellet dust is not preferred in blast furnace processes of integrated iron and steel plants. Pellet dust reduces the gas permeability of the blast furnace (Das et al 2001; Mumme 2003). Therefore, the pellet material is screened before being fed into the blast furnace process. In sinter production, pellet dust is added to the sinter mixture in the dosing unit. The current study investigated the effects of using pellet dust instead of iron ore in sinter blend on SFCA phases. Table 2 shows the chemical composition and dimensions (mm) of Iron ore (A) (%) and Iron Ore (A) pellet dust. Sinter tests were carried out only by changing the usage ratios of iron ore (A) and iron ore (A) pellet dust in the sinter mixture (Table 3). Other auxiliaries (coke dust, waste materials, fluxes, etc.) were left at fixed proportions. Equal amounts of sinter blends were used in all experiments. It has been necessary to add flux materials to regulate the basicity of the sinter mixture (mass CaO% / mass SiO₂%) up to 1.90. Table 4 shows the chemical analysis of five sinter samples.

Table 2
Chemical composition (mass %) and cumulative undersize (mm) values of iron ore (A) and iron ore (A) pellet dust

Chemical composition (%)	T Fe	SiO₂	Al₂O₃	Fe₂O₃	CaO	MgO	K₂O	Na₂O	P	TiO₂
<i>Iron ore (A) (%)</i>	66.3	2.48	1.33	94.8	0.11	0.033	0.21	0.013	0.038	0.091
<i>Iron Ore (A) pellet dust (%)</i>	66.1	3.3	1.58	94.3	0.22	0.07	0.22	0.029	0.042	0.014
<i>Cumulative undersize (mm)</i>	10	8.0	6.3	5.0	4.0	3.0	2.0	1.0	0.5	0.3
<i>Iron ore (A) (%)</i>	100	94.46	78.72	69.22	57.20	47.69	28.68	12.26	5.16	5.22
<i>Iron Ore (A) Pellet dust (%)</i>	100	100	100	98.43	81.93	65.42	20.63	2.95	0.00	0.00

Table 3
Raw material utilization in the sinter blends (mass %).

Raw materials	Sin-1	Sin-2	Sin-3	Sin-4	Sin-5
<i>Main Iron Ore</i>	33.80	33.26	32.90	32.61	31.90
<i>Iron ore (A)</i>	23.15	13.67	9.02	4.47	0.00
<i>Iron Ore (A) Pellet dust</i>	0.00	9.11	13.53	17.88	21.86
<i>Iron bearing dusts</i>	22.53	24.65	25.12	25.98	28.21
<i>Total Flux makers</i>	15.62	14.66	14.78	14.35	13.70
<i>Total Fuel</i>	4.90	4.65	4.65	4.71	4.32
<i>Total Sinter Blend (%)</i>	100.00	100.00	100.00	100.00	100.00

Table 4
Chemical analysis of sinter samples (mass %).

Chemical analysis	Sin-1	Sin-2	Sin-3	Sin-4	Sin-5
<i>Fe(tot)</i>	54.70	55.05	55.90	55.10	54.40
<i>FeO</i>	6.53	6.85	7.49	7.55	7.25
<i>CaO</i>	11.80	11.45	11.10	11.40	11.34
<i>MgO</i>	1.69	1.71	1.66	1.65	1.79
<i>SiO₂</i>	5.63	5.85	5.46	5.96	5.82
<i>Al₂O₃</i>	1.48	1.51	1.39	1.56	1.46
<i>K₂O + Na₂O</i>	0.29	0.27	0.24	0.28	0.31
<i>MnO</i>	0.93	0.88	0.74	0.84	0.94

In this study, sinter samples were analyzed using the X'Celerator detector and Panalytical X'Pert Pro dust diffractometer in Fe filtered Co-K α radiation ($\lambda = 1.789\text{\AA}$) environment. Phase structures of sinter samples were defined using Panalytical X'Pert Highscore plus software, and quantitative measurements were performed with Autoquan/BGMN software. Figure 2 shows the preparation of the sintered sample for X-ray diffraction analysis.

XRD analyzes were used to measure the mass fraction of various phase structures in the sinter samples and the different iron ore (A) pellet dust fractions in the sinter mix. Table 5 summarizes the XRD analyzes.

Figure 3 shows the XRD quantity measurement of sinter samples formed with distinct pellet dust ratios. The variation of the pellet dust size of the sinters was observed to affect the rate of the various sinter phase structures in the sintering process. When the utilization rates of iron ore (A) and iron ore (A) pellet dust particles vary between 0% (Sin-1) to 21.86% (Sin-5), the different sinter phases show specific trends in the sinter samples.

The results of X-ray diffraction and mineralogical studies on sinter samples containing different proportions of micro pellet fraction showed sinter samples in distinct mineralogical structures. The current study investigated magnetite (Fe₃O₄), hematite (Fe₂O₃), larnite-C₂S (Ca₂SiO₄), SFCA (M₁₄O₂₀), SFCA-I (M₂₀O₂₈), wuestite (FeO) phases using X-ray diffraction. Figure 3 shows the results.

The XRD values show an insignificant difference in the chemical composition of iron ore (A) pellet dust and iron ore (A). This finding shows no chemical component difference exists between iron ore (A) and pellet dust but only a difference arising from the morphological structures in the sinter. Moreover, XRD results show that pellet dust sinter contains more hematite, magnetite, SFCA, and lower SFCA-I than normal sinter.

Results And Discussion

Chemical, optical and mineralogical analyzes of the sinter samples were carried out to determine the sinter structures in the sinter samples. Table 4 shows the results of the sinter laboratory studies. The sintered compound's construction varies depending on the particle size, chemical composition of iron ore, fluxes, and the extent of the reactions (Goldring et al. 1989; Lu and Ishiyama 2015). Sinter production consists of many phases and especially SFCA and SFCA-I compositions. These different phases occur depending on the operational and processual conditions of the sinter. The mineralogical formation has a significant effect on softening and melting temperature (Pal et al. 1998).

Effects of pellet dust on sinter phase composition.

The mineralogical structure of the sinter was investigated using the dust diffraction technique (rietveld method). Quantification of calcium and aluminum silicoferites (SFCA) and calcium silicates (larnite) determines the strength of sinter materials and the return rate of fine dusts. Table 5 shows the mineralogical compounds and results of several produced sinter samples.

Table 5
Quantitative XRD analysis of sinter productions (%).

<i>Phases</i>	<i>Sin-1</i>	<i>Sin-2</i>	<i>Sin-3</i>	<i>Sin-4</i>	<i>Sin-5</i>
<i>Larnite</i>	7.65	7.27	7.42	6.70	6.83
<i>Hematite</i>	25.43	28.63	24.04	23.08	28.52
<i>Magnetite</i>	27.89	26.60	27.54	32.67	27.22
<i>SFCA-I</i>	16.20	15.39	16.01	14.36	10.30
<i>SFCA</i>	22.84	21.17	24.99	22.17	27.13
<i>Total SFCA</i>	39.04	36.56	41.00	36.53	37.43
<i>SFCA-I/SFCA</i>	0.71	0.73	0.64	0.65	0.38
<i>Wuestite</i>	0.00	0.96	0.00	1.02	0.00

When iron ore (A) was replaced with iron ore (A) pellet dust, the columnar SFCA phase in the sinter somewhat improved and reached a maximum value of 27.13% (Sin-5) (Fig. 5). The pellet dust in the sinter blend creates regions of high density, resulting in higher assimilation ability (Honeyands et al. 2019). The sintering mixture containing 13.53% pellet dust fraction (Sin-3) probably reached the maximum assimilation reaction rate and produced higher SFCA and SFCA-I values. When the particle size of the pellet dust is over 13.53%, the reduction of the reaction area results in poor assimilation reactions and thus poor values of SFCA-I.

The sinter pot test revealed the SFCA-I/SFCA correlation comparatively. Correlation is crucial for sintering carried out with fine iron ore. The SFCA-I/SFCA value ratio decreased from 0.71 (Sin-1) to 0.38 (Sin-5),

depending on the iron ore (A) pellet dust fraction in the sinter mixture (Fig. 6). It can be said that SFCA-I compulsion shapes with similitude of pellet grains. Hida et al. (1983) declared that, meanwhile another models of SFCA are consisted of the fusing stage.

As seen in Fig. 7, while the hematite phase in the sinter formation increases, the SFCA + SFCA-I phases decrease. There is a complete contrast between the hematite and the other phases in the sinter matrix.

Replacing fine iron ore with pellet dust particles differed the sintering rate and SFCA-I. The sinter blend with 0% fine iron ore fraction (Sin-1) had the highest sintering rate and SFCA-I (25.25 mm/min, 16.20%, respectively), while the sinter mix with 21.86% fine iron ore fraction (Sin-5) has the lowest sintering rate and SFCA-I (21.20 mm/min, 10.30% respectively). However, the SFCA value increased from 22.17–27.13% due to the rising fine iron ore in the sinter mixture (Fig. 8). This situation suggests that the replacement of coarse ore with fine iron ore reduces airflow rate and slows the flame front across the sinter bed (FFS: flame front speed). With the reduction of the average particle size of the iron ore, the airflow velocity in the sintered body decreased. As a result, it was observed that the sintering efficiency and sintering rate decreased. The higher the coarse ore content in the sinter bed, the greater the sintering rate.

Figure 9 shows the variation in sintering time depending on the amount of SCA and SFCA-I. Replacing fine iron ore with pellet dust particles increased sintering time and SFCA. Sinter mix with 0% fine iron ore fraction (Sin-1) has the lowest sintering time and SFCA (19.80 min, 22.84%, respectively), while 21.86% fine fraction mix (Sin-5) has the highest sintering time and SFCA (25.90 min, 27.03%, respectively). However, the SFCA-I value decreased from 15.36–10.30% due to the increase in fine iron ore in the sinter mix (Fig. 9). This situation shows that the replacement of coarse ore with fine iron ore increases the sintering time and quantity of SFCA in the sinter.

Optical microscopy analysis of the sinter formation

The sintering process contains a lot of chemical reactions during sinter production. These reactions form several compounds in the sintered material (Dawson 1993). The temperature distribution varies in the sintered material, and some cracks occur around the magnetite compound. These cracks and pores affect the physical properties of the sintered product (Webster et al. 2013; Hida et al. 1983; Dawson et al. 1984; Honeyands et al. 2017). Different compounds occur in different amounts depending on the basicity of the mixing material and the cooling rate. Through the distinct reflections obtained from sinter phases, microscopic analysis revealed that the sinter matrix usually consisted of secondary magnetite and hematite grains (settled from primary sinter melt), flux grains, and complex calcium ferrites known as Silicoferrite Calcium and Aluminum (SFCA), glass and silicate (e.g., larnite, Ca_2SiO_4). Figure 10 shows optical micrographs of the major sinter phases. In the microscope research on sinter material, hematite, magnetite, and SFCA phases are seen among other sinter phases with different reflections. A glowing compound may be hematite and found right next to the gray SFCA phase. These phases can be in heterogeneous textures within the industrial sinter material.

The replacement of fine iron ore (A) fractions with iron ore (A) pellet dust resulted in the sinter formation with more magnetite, hematite, SFCA, and less larnite and SFCA-I. Pellet dust fractions are more reactive than the iron ore particle and provide more softening in solid grains.

Figure 10(a) shows the sintered microstructure containing 0% pellet dust (Sin-1). It has been observed that sinter reactions occur in the SFCA bond phase formation. The sin-1 sample comprises fine, acicular tissue of SFCA and hematite. Here, fine magnetite crystal grains and several interlaced hematite growths are seen. The Sin-2 sample, a sinter blend containing 9.11% iron ore (A) pellet dust, could be argued to start the recovery with hematite, magnetite, SFCA phases, and SFCA-I appearing in the sintered sample. The sin-3 sintered sample containing 13.53% pellet dust fraction produced the best phase result in hematite, magnetite, and especially SFCA and SFCA-I (24.99% and 16.01%, respectively).

As shown in Fig. 10, when the pellet dust ratio rose above 17.88% in Sin-4 and Sin-5 samples, the hematite, magnetite, and SFCA phase increased in the sinter, but SFCA-I decreased (Figs. 10d-10e). This situation may be due to increased cracking and stresses in contact with pellet dust particles during the compaction and reaction of the sinter mixture. Figures 10a, 10b, and 10e (Sin-1, Sin-2, and Sin-5, respectively) show optical micrographs of SFCA and multiporous SFCA-I phases.

It can be observed more hematite, magnetite, and different SFCA types. Sinter samples have no clear differentiation between flat and blocky SFCA. Most of the bonding structure is considered blocky SFCA. Recent studies revealed that acicular SFCA could appear flat and be easily confused with blocky SFCA in these phases. Therefore, the correct classification of the different SFCA types requires utilizing other analytical methods (Tonžetić and Dippenaar 2011).

SEM study on the sinter formation

SEM analyzes were performed on O, Mg, Al, Si, K, Ca, Mn, and Fe elements to identify sinter patterns. Larnite-C₂S, wuestite, hematite, magnetite, and SFCA phases were analyzed and identified through optical microscopy. Approximately 510 SEM-EDS analyzes were performed on equally shining parts of the five different sinter samples to identify and learn the chemical composition of the different phase structures. Results were collected according to elemental analysis and then compared with the literature to reveal the chemical composition of the phases (especially for the different types of SFCA phases).

After a detailed investigation of iron ore sintering, Pownceby et al. (2016) declared that general chemical analysis of sinters could not be performed by only characterizing microstructures, considering each phase in the sinter might have a significant variation in the chemical composition (Goldring 1989). Each phase may appear in different morphologies. Figures 11(c), 11(d), and 11(e) show typical micrographs of SFCA and SFCA-I. Columnar SFCA has less microporosity than acicular SFCA in these micrographs. Columnar SFCA appears to be more associated with other melt phases, such as hematite, magnetite, and glass (Figs. 11(a), 11(c), 11(e)). Acicular SFCA and columnar SFCA phases have formed at a lower temperature through a solid-state reaction between fine iron ore grains and pellet dust particles. SEM analysis has

shown that columnar SFCA has the same chemical composition as acicular SFCA but different morphology.

Figure 11 shows the morphological structure of the different phases in the sintered material. Hematite, magnetite, and SFCA phases were recognized in the sinter. The segregation between several types of SFCA was not clear. This situation might have stemmed from very few chemical differences between the SFCA phases. The composition of the SFCA phases was similar to each of SFCA and SFCA-I. The morphology of the sintered material is mainly associated with the composition mode and is related to its specific chemical composition, heating, and cooling rate. Therefore, comparing the chemical compound with those in the literature can help to reveal various SFCA structures.

While SFCA develops slowly and persists longer at low temperatures, it develops and disappears rapidly at high temperatures (Lu 2015; Egundebi and Whiteman 1989; Bai et al. (2019); Turriff 2007). The authors explained that the length of time at sintering is a significant factor in the amount of SFCA produced. Most scientists suggest that slower sintering at lower temperatures will yield more SFCA than sintering at higher temperatures. EDS analyses from stoichiometry calculations of the analyzed SFCA phases did not allow for an obvious distinction between the two SFCA types based on $M_{14}O_{20}$ (SFCA) and $M_{20}O_{28}$ (SFCA-I) phases (Honeyands et al. 2017; Tonžetić et al. 2011).

Morphological features of SFCA

As shown in Fig. 12, SFCA can be divided into three types of morphological structures, depending on their character traits: blocky type (SFCA), acicular type (SFCA-I), and dendritic type (SFCA-II). Dendritic type SFCA was not in the area of interest of this study. The chemical composition and morphology of two types of SFCA were investigated. The blocky type SFCA was observed to have lower Fe_2O_3 content than the platy type but higher Ca and Si. There was no significant difference in the amount of Al_2O_3 between the two structures. SFCA of the columnar type had a lower MgO than the acicular type.

In conclusion, increasing the liquid phase content in the softening zone and developing a bonding structure chiefly composed of blocky and platy SFCA seems effective in increasing the strength.

As shown in Fig. 13, EDS analyses of SFCA structures were performed on the Al_2O_3 -CaO- Fe_2O_3 triple-phase. This phase diagram was used to position hematite, magnetite, SFCA, and SFCA-I mineral compounds in the sintered material. The chemical compounds of the SFCA phases appeared to be close to SFCA and SFCA-I. Figure 13 shows SFCA, SFCA-I, and SFCA-II in a series of solid solutions of SFCA. The results of the EDS analysis on the SiO_2 -CaO- Fe_2O_3 and Si-Ca-Fe phase diagrams are shown in Figs. 12, 13, and 14. It was also observed that the replacement of iron ore (A) pellet dust with Iron Ore (A) gradually transferred most of the chemical compounds of SFCA toward the SFCA-I region (Figs. 13 and 14). This situation may confirm the results of XRD spotting that high pellet dust fractions in the sinter support SFCA formation rather than platy SFCA-I (Ji et al. 2019; Wang et al. 2019; Liao and Guo 2019; Zhang et al. 2019).

The shaded region in Fig. 14 shows that most SFCA compounds are intertwined in industrial sintering. Pownceby and Clout (2003) reported that SFCA and SFCA-I form in a range of solid solutions of SFCA (Kahlenberg et al. 2021; Zöll et al. 2018). Different relative ratios of SFCA models can coexist depending on the sinter parameters (e.g., oxygen potential) and physical properties (particle size, porosity, etc.), and the chemical composition of the raw materials.

In this study, approximately 510 SEM-EDS analyzes were performed on five sinter samples. All compositions of sinter samples were marked with dots representing microprobe data. Figure 15 shows the color distribution of Si/Ca/Fe elements, which are necessary for determining the SFCA and SFCA-I phase structures in the sintered microstructure. The key element map of SFCA showed the sintered particle color distribution as Si, Ca, and Fe. Figure 15 shows the relevant map of elements using the Thermo Scientific- FEI Apreo S equipped with an Ultra Dry EDS Detector and Quasor II EBSD. This image shows all the recognized phases in the sintered material containing the SFCA type.

Figure 16(a) shows microprobe map analyses displaying phase mineralogy and textures developed from sinter samples. Here, the first cluster (blue) represented a mixture of hematite and magnetite phases, the second cluster (red) the SFCA-I phase structure, and the third cluster (green) the SFCA phase formation. The region between (1) one number (blue) and (2) two number (red) might be a different phase structure in the sintered material (Fig. 16(a)). Magnetite and SFCA-I were close to each other in the (2) two number region because of their similar chemical composition and color texture. Therefore, it was difficult to distinguish them from one another by the microscope and the SEM-EDS method. The chemical morphologies of the SFCA models were characterized. The results showed that the SFCA structures were similar to chemical compounds for which they were identified in the literature. Figure 16(b) is the key element map of SFCA showing the distribution of sinter particle color of Si, Ca, and Fe. The phase patched map showed the distribution of all phases in the sintered material. SFCA was chiefly related to magnetite, while SFCA-I was mainly to hematite.

Chemical analysis of Ca-Si-Al-Fe elements in total sinter samples

SEM and EDS spectrum analyzes of sintered samples were performed. In order to determine the chemical composition of SFCA phase types, 602 SEM-EDS analyzes were performed on five sinter samples. Among the O, Mg, Al, Si, K, Ca, Mn, and Fe elements, Fe, Si, Ca, and Al were selected from Figs. 17 to 20 show the analysis results.

Figure 18 shows that the phases containing 0.5–5% Si could be SFCA and SFCA-I. The ones with less than 0.5% Si may be hematite, magnetite, etc., while the phases containing over 5% Si are possibly larnite phase formations. In this investigation, approximately 79% of the total SFCA phases in the sinter samples included Si in proportions ranging from 2.5–5%. Roughly 85% of the SFCA-I phases in the sinter contained Si ratios ranging from 0.5–2.5%.

Figure 19 shows that the phases with 6–12% Ca can be SFCA and SFCA-I. Phases containing less than 6% Ca may be hematite, magnetite, etc. Phases containing more than 12% Ca may be the larnite phase

formation. In this study, almost 75% of the total SFCA phases in the sinter had Ca between 9–12%. Approximately 80% of the SFCA-I phases in the sinter samples possessed Ca in proportions ranging from 6–9%.

Figure 20 shows that the phases containing 0–1% Al will exhibit hematite and magnetite structure rather than SFCA and SFCA-I. Phases containing 1–3% Al will demonstrate an SFCA structure rather than SFCA-I. In this study, almost 66% of the total SFCA phases in the sinter contained Al in proportions ranging from 1.5–3%. Approximately 54% of the SFCA-I phases in the sinter had Al content ranging from 0–1.5%.

Particle size of phases in the sintered material

SFCA phase structures in sinter were investigated by optical microscope and SEM analysis. Elemental values of the phases were determined with the EDS analysis method. The grain size of the phases in the sinter was performed using the Image J program. Depending on the size of the crystals, SFCA (silico-ferrite of calcium and aluminum) phases can develop as dendritic SFCA, flat SFCA, and columnar SFCA. As a result of the tests performed in this study were determined that more than 32% of the total SFCA consisted of platy SFCA (SFCA-I). The relationship between fine iron ore particle size and the formation of sinter phases during the sinter tests is summarized in Fig. 21.

In Fig. 21, considering the grain size smaller than 26 microns, the phases should be SFCA and SFCA-I. Especially, grain sizes smaller than 16 microns may contain more SFCA-I phase. Grain sizes larger than 26 microns may have more hematite, magnetite, etc.

Conclusions

The current study investigated the effects of iron ore (A) pellet dust, sintering time, sintering rate, phase content (especially SFCA, SFCA-I), and basicity on sintering morphology, quality, optical and microprobe properties of iron ore sinters. Microscopic, XRD, SEM-EDS, chemical, and particle-based phase analyses were performed to examine the physical and metallurgical quality properties of sintered samples. The sinter quality was investigated according to the sintering morphology, which depends on the chemical composition of the sintering blend. According to XRD analyses, total SFCA phase ratios in sinter samples decreased slightly with increasing iron ore (A) pellet dust fraction (Tables 3 and 5). The SFCA phase did not significantly affect when the proportion of iron ore (A) pellet rose from 0% (Sin-1) to 17.88% (Sin-4), but SFCA-I dropped from 16.20% (Sin-1) to 14.36%. The SFCA phase increased up to 27.13% (Sin-5), with an additional increase in the percent iron ore (A) pellet dust fraction (Table 5 and Fig. 5). Replacing the iron ore (A) pellet dust with iron ore (A) in the iron ore blend affected the formation of both the platy SFCA (SFCA-I) and the blocky SFCA phase (SFCA). The chemical compositions of the analyzed SFCA phases were then plotted on the Al_2O_3 - SiO_2 - CaO - Fe_2O_3 and Si-Ca-Fe triple-phase system plane (Figs. 13–16). These compounds of SFCA were in the vicinity of the SFCA and SFCA-I sites. It was found that the SFCA-I/SFCA ratio decreased from 0.71 (Sin-1) to 0.38 (Sin-5) with an increase in iron ore (A) pellet fraction in sinter samples (Fig. 6). Replacing fine iron ore with pellet dust particles worsened the sintering rate and SFCA-I structure (Fig. 8) but increased the sintering time (Fig. 9).

In this study, it was significant to meet an optimal between mineral compound and sinter property which conforms to the commonly adopted characterization. The Sin-3 sinter obtained with a fine ore particle size of 13.53% has ideal properties that meet the definitions required by the blast furnace (Table 5, Figs. 5 and 7). Reflected light microscopy and SEM investigation demonstrated that platy and blocky SFCA could not be clearly recognized using EDS examination and measuring $M_{14}O_{20}$ and $M_{20}O_{28}$ stoichiometries of phase structures. In this study, more than approximately 32% of total SFCA consisted of acicular SFCA (SFCA-I) (Fig. 21). The chemical compounds of the SFCA phase structures moved towards the SFCA-I hollow due to the increased rate of iron ore (A) pellet dust in the sinter mixture.

Declarations

Acknowledgments The author wishes to thank Prof. Dr. Johan P.R. De Villiers from the Department of Materials Science and Metallurgical at the University of Pretoria, The Republic of South Africa for all of his bits of help in reading mineralogical phases and interpretation assistance. The author also thanks to 2219 Research Scholarship and Supports Directorate (BİDEB) of The Scientific and Technological Research Council of Turkey (TUBITAK) for support.

Author contribution The author contributed to the study's conception and design. Characterization and measurements, data collection, formal analysis, and material preparation were performed and written by Ömer Saltuk Bölükbaşı. The author read and approved the final manuscript.

Funding Not applied

Availability of data and materials All data presented in the text of the article are fully available without restriction from the author upon request. Code availability is not applicable.

Ethics approval This study follows the "European Code of Conduct for Research Integrity" as well as the "Ethics for Researchers" guideline of the European Commission.

Consent to participate Author consent to participate in this study.

Consent for publication Author consent for publication of this study.

Conflicts of interest No conflicts of interest/No competing interests.

Open Access This article is licensed under a Creative Commons Attribution 4.0 International License, which permits use, sharing, adaptation, distribution and reproduction in any medium or format, as long as you give appropriate credit to the original author(s) and the source, provide a link to the Creative Commons licence, and indicate if changes were made. The images or other third party material in this article are included in the article's Creative Commons licence, unless indicated otherwise in a credit line to the material. If material is not included in the article's Creative Commons licence and your intended use is not permitted by statutory regulation or exceeds the permitted use, you will need to obtain permission

directly from the copyright holder. To view a copy of this license, visit <http://creativecommons.org/licenses/by/4.0/>.

References

1. Bai K, Shen J, Zhu Z, Zuo H, Pan Y, Wang J, Xue Q (2019) Effect of Al_2O_3 on the Formation of Calcium Ferrite in the Solid. *State Metals* 9(6) 681. <https://doi.org/10.3390/met9060681>
2. Cai B, Watanabe T, Kamijo C, Susa M, Hayashi M (2018) Comparison between reducibilities of columnar silico-ferrite of calcium and aluminum (SFCA) covered with slag and acicular SFCA with fine pores. *ISIJ Int* 58(4) 642-651. <https://doi.org/10.2355/isijinternational.ISIJINT-2017-552>
3. Das AK, Kumar A, De AK, Mukherjee T (2001) 60th Ironmaking conf. Proc., Iron & Steel Society, Warrendale. PA USA 973
4. Dawson PR (1993) Recent development in iron ore sintering. II. Research studies on sintering and sinter quality *Ironmak Steelmak (UK)* 20(2) 137-143. <https://doi.org/10.1080/03719553.2016.1165500>
5. Dawson PR, Ostwald J, Hayes KM (1983) The influence of the sintering temperature profile on the mineralogy and properties of iron ore sinters. In *AIMM Bull Proc Vol. 289 No. 5* 163-169. <https://doi.org/10.2355/isijinternational.53.1334>
6. Dawson PR, Ostwald J, Hayes KM (1984) The influence of the sintering temperature profile on the mineralogy and properties of iron ore sinters. *Proc Aust Inst Min Metall Proc Vol. 289 No. 5* 163-169
7. De Villiers JPR, Verryn SMC (2008) Ninth International Congress for Applied Mineralogy. Brisbane, QLD. September 8-10, 265–275
8. Egundebi GO, Whiteman JA (1989) Evolution of microstructure in iron-ore sinters. *Ironmak Steelmak* 16(6) 379-385
9. Fernández-González D, Piñuela-Noval J, Verdeja LF (2018) Iron ore agglomeration technologies. *Iron ores and iron oxide materials. Intechopen Londres* 61-80. <http://dx.doi.org/10.5772/intechopen.72546>
10. Fernández-González D, Ruiz-Bustanza I, Mochón J, González-Gasca C, Verdeja LF (2017) Iron ore sintering: Process Miner. *Process Extr Metall Rev* 38(4) 215-227. <https://doi.org/10.1080/08827508.2017.1288115>
11. Garbers-Craig AM, Geldenhuis JMA, Jordaan WJ, Pistorius PC (2003) The influence of increased air flow on the spatial variation of iron sinter quality. *J South Afr Inst Min Metall* 103(10) 645-650. https://hdl.handle.net/10520/AJA0038223X_2970
12. Goldring DC, Jukes LM, Fray TAT (1989) Characterization of Iron Ore Sinter from its Mineralogy. *Institute of Chemical Engineers, 5th International Symposium on Agglomeration, Brighton, UK; 25-27 Sept.*, 425-429
13. Hamilton JG, Hoskins BF, Mumme WG, Borbidge WE, Montague MA (1989) The crystal structure and crystal chemistry of $\text{Ca}_{2.3}\text{Mg}_{0.8}\text{Al}_{1.5}\text{Si}_{1.1}\text{Fe}_{8.3}\text{O}_{20}$ (SFCA): solid solution limits and selected phase

- relationships of SFCA in the SiO₂-FeO₃-CaO (-Al₂O₃) system. *Neues Jahrbuch für Mineralogie. Abhandlungen* 161(1) 1-26
14. Hida Y, Ito K, Sasaki M, Umezu Y (1983) Effect of the mineralogical properties of coarse ores on the reducibility and the productivity of sinter. *Trans. ISIJ* vol. 23, 33-35
 15. Honeyands T, Manuel J, Matthews L, O’dea D, Pinson D, Leedham J, Donskoi E (2019) Comparison of the mineralogy of iron ore sinters using a range of techniques. *Miner* 9(6) 333. <https://doi.org/10.3390/min9060333>
 16. Honeyands T, Manuel J, Matthews L, O’dea D, Pinson D, Leedham J, Pownceby MI (2017) Characterising the mineralogy of iron ore sinters. *State-of-the-art in Australia, Proc Iron Ore* 49-60
 17. Hsieh LH, Ja W (1989) Effect of oxygen potential on mineral formation in lime-fluxed iron ore sinter. *ISIJ Int* 29(8) 625-634. <https://doi.org/10.2355/isijinternational.29>
 18. Ji Z, Zhao Y, Gan M, Fan X, Chen X, Hu L (2019) Microstructure and Minerals Evolution of Iron Ore Sinter: Influence of SiO₂ and Al₂O₃. *Miner* 9(7) 449. <https://doi.org/10.3390/min9070449>
 19. Kahlenberg V, Krüger H, Tribus M, Anwander B (2021) SFCA-II type Ca_{2.46}Fe³⁺_{8.57}Fe²⁺_{0.52}Al_{5.45}O₂₄⁻ an improved structural model for an iron-ore sinter phase. *Mineralogy and Petrology*, 115(1), 137-147. <https://doi.org/10.1007/s00710-020-00730-y>
 20. Kalenga MK, Garbers AM (2008) Investigation into the influence of magnesia content, alumina content, basicity and ignition temperature on the mineralogy and properties of iron sinter. (Doctoral dissertation, University of Pretoria)
 21. Koryttseva A, Webster NA, Pownceby MI, Navrotsky A (2017) Thermodynamic stability of SFCA (silico-ferrite of calcium and aluminum) and SFCA-I phases. *J Am Ceram Soc* 100(8) 3646-3651. <https://doi.org/10.1111/jace.14857>
 22. Liao F, Guo XM (2019) The Effects of Al₂O₃ and SiO₂ on the Formation Process of Silico-Ferrite of Calcium and Aluminum (SFCA) by Solid-State Reactions. *Miner* 9(2) 101. <https://doi.org/10.3390/min9020101>
 23. Lister DH, Glasser FP (1967) Phase relations in the system CaO-Al₂O₃-iron oxide. *Brit Ceram Soc Trans* 66(7) 293-305
 24. Loo CE (1998) Some progress in understanding the science of iron ore sintering. In 2nd International Congress on the Science and Technology of Ironmaking and 57th Ironmaking Conference, Warrendale, USA 1299-1316
 25. Loo CE, Wan KT, Howes VR (1988) Mechanical-Properties of Natural and Synthetic Mineral Phases in Sinters Having Varying Reduction Degradation. *Indices Ironmak Steelmak* 15(6) 279-285
 26. Lu L (2015) Important iron ore characteristics and their impacts on sinter quality-a review. *Min Metall Explor* 32(2) 88-96
 27. Lu L, Ishiyama O (2015) Iron ore sintering. In *Iron Ore Woodhead Pub* 395-433. <https://doi.org/10.1016/B978-1-78242-156-6.00014-9>

28. Lv X, Bai C, Deng Q, Huang X, Qiu G (2011) Behavior of liquid phase formation during iron ores sintering. *ISIJ Int* 51(5) 722-727. <https://doi.org/10.2355/isijinternational.51.722>
29. Mitra K, Nath NK (2005) Analysis of two-layer sintering process for different bed heights by genetic algorithm. *IFAC Proc Vol.* 38(1) 63-68. <https://doi.org/10.3182/20050703-6-CZ-1902.016>
30. Mumme WG (2003) The crystal structure of SFCA-II, $\text{Ca}_{5.1}\text{Al}_{9.3}\text{Fe}^{3+}_{18.7}\text{Fe}^{2+}_{0.9}\text{O}_{48}$ a new homologue of the aenigmatite structure-type, and structure refinement of SFCA-type, $\text{Ca}_2\text{Al}_5\text{Fe}_7\text{O}_{20}$. Implications for the nature of the Neues Jahrbuch für Mineralogie-Abhandlungen *J. Mineral. Geochem.* 178(3) 307-335. Doi:10.1127/0077-7757/2003/0178-0307
31. Mumme WG, Clout JMF, Gable RW (1998) The crystal structure of SFCA-I, $\text{Ca}_{3.18}\text{Fe}^{3+}_{14.66}\text{Al}_{1.34}\text{Fe}^{2+}_{0.82}\text{O}_{28}$, a homologue of the aenigmatite structure type, and new crystal structure refinements of β -CFF, $\text{Ca}_{2.99}\text{Fe}^{3+}_{14.30}\text{Fe}^{2+}_{0.55}\text{O}_{25}$ and Mg-free SFCA, $\text{Ca}_{2.45}\text{Fe}^{3+}_{9.04}\text{Al}_{1.74}\text{Fe}^{2+}_{0.16}\text{Si}_{0.6}\text{O}_{20}$ Neues Jahrbuch für Mineralogie-Abhandlungen. 93-117. DOI: 10.1127/njma/173/1998/93
32. Nicol S, Chen J, Pownceby MI, Webster NA (2018) A Review of the Chemistry, Structure and Formation Conditions of Silico-Ferrite of Calcium and Aluminum (SFCA) Phases. *ISIJ Int* 58(12) 2157-2172. <https://doi.org/10.2355/isijinternational.ISIJINT-2018-203>
33. Nyembwe MA (2012) Study of sinter reactions when fine iron ore is replaced with coarse ore, using an infrared furnace and sinter pot tests. (Doctoral dissertation, University of Pretoria).
34. Pal S, Chandra N, Mishra UN, Singh RN, Mediratta SR (1998) Effect of mineralogical composition of iron-bearing materials on softening-melting properties. In 2nd International Congress on the Science and Technology of Ironmaking and 57th Ironmaking Conference, 1615-1621
35. Pownceby MI, Clout JMF (2003) Importance of fine ore chemical composition and high temperature phase relations: applications to iron ore sintering and pelletising. *Miner. Process Extr Metall* 112(1) 44-51. <https://doi.org/10.1179/037195503225011402>
36. Pownceby MI, Webster NAS, Manuel JR, Ware N (2016) The influence of ore composition on sinter phase mineralogy and strength *Miner Process Extr Metall* 125(3), 140-148. <https://doi.org/10.1080/03719553.2016.1153276>
37. Sasaki M, Hida Y (1982) Consideration on the Properties of Sinter from the Point of Sintering Reaction. *Tetsu-to-Hagané.* 68(6) 563-571. https://doi.org/10.2355/tetsutohagane1955.68.6_563
38. Scarlett NV, Pownceby MI, Madsen IC, Christensen AN (2004) Reaction sequences in the formation of silico-ferrites of calcium and aluminum in iron ore sinter. *Metall Mater Trans B*, 35(5), 929-936. <https://doi.org/10.1007/s11663-004-0087-4>
39. Scarlett NV, Pownceby MI, Madsen IC, Christensen AN (2004) Reaction sequences in the formation of silico-ferrites of calcium and aluminum in iron ore sinter. *Metall Mater Trans B* 35(5) 929-936. <https://doi.org/10.1007/s11663-004-0087-4>
40. Tonžetić I, Dippenaar A (2011) An alternative to traditional iron-ore sinter phase classification. *Miner Engin* 24(12) 1258-1263. <https://doi.org/10.1016/j.mineng.2011.04.012>

41. Turriff DMR, (2007) Process Kinetics of Transient Liquid Phase Sintering in a Binary-Isomorphous Alloy System. PhD Thesis, University of Waterloo, Ontario, Canada, 65-135.
<https://doi.org/10.3390/met9060681>
42. Van Den Berg T (2008) An assessment of the production of fine material in iron ore sinter. (Doctoral dissertation, University of Pretoria).
43. Van Den Berg T, De Villiers JPR (2009) An assessment of the production of fine material in iron ore sinter Process. *Extr Metall* 118(4) 214-221. <https://doi.org/10.1179/174328509X455313>
44. Wang W, Yang D, Ou-Yang Z, Xu R, Song M (2019) Effect of SiO₂ on the Formation of Acicular Calcium Ferrite in Sinter. *Metall Mater Trans B* 50(2) 678-687. <https://doi.org/10.1007/s11663-019-01528-w>
45. Webster NA, Churchill JG, Tufaile F, Pownceby MI, Manuel JR, Kimpton JA (2016) Fundamentals of silico-ferrite of calcium and aluminium (SFCA) and SFCA-I iron ore sinter bonding phase formation: Effects of titanomagnetite-based ironsand and titanium addition. *ISIJ Int* 56(10) 1715-1722.
<https://doi.org/10.2355/isijinternational.ISIJINT-2016-162>
46. Webster NA, Pownceby MI, Madsen IC (2012) Kimpton JA Silico-ferrite of calcium and aluminum (SFCA) iron ore sinter bonding phases: new insights into their formation during heating and cooling. *Metall Mater Trans B* 43(6) 1344-1357. <https://doi.org/10.1007/s11663-012-9740-5>
47. Webster NA, Pownceby MI, Madsen IC (2013) In situ X-ray diffraction investigation of the formation mechanisms of silico-ferrite of calcium and aluminium-I-type (SFCA-I-type) complex calcium ferrites. *ISIJ Int* 53(8) 1334-1340. <https://doi.org/10.2355/isijinternational.53.1334>
48. Webster NA, Pownceby MI, Pattel R (2017) Fundamentals of silico-ferrite of calcium and aluminium (SFCA) and SFCA-I iron ore sinter bonding phase formation: Effects of mill scale addition. *Powder Diffr* 32(2) 85-89. <https://doi.org/10.1017/S088571561700080X>
49. Wei R, Lv X, Yang M, Xu J, You Z (2018) Improving the property of calcium ferrite using a sonochemical method. *Ultrason Sonoch.* 43 110-113. <https://doi.org/10.1016/j.ultsonch.2018.01.008>
50. Yang LX, Matthews E (1997) Sintering reactions of magnetite concentrates under various atmospheres. *ISIJ Int* 37(11) 1057-1065. <https://doi.org/10.2355/isijinternational.37.1057>
51. Zhang X, Bai H, Lu X, T He, Zhang J, Yuan H, Zhang Z (2019) Effect of Cooling Methods on the Strength of Silico-ferrite of Calcium and Aluminum of Iron Ore Sinter during the Cooling Process. *Metals.* 9(4) 402. <https://doi.org/10.3390/met9040402>
52. Zöll K, Kahlenberg V, Krüger H, Tropper P (2018) Investigations on FCAM-III (Ca_{2.38}Mg_{2.09}Fe_{10.61}³⁺Fe_{1.59}²⁺Al_{9.33}O₃₆): a new homologue of the aenigmatite structure-type in the system CaO-MgO-Fe₂O₃-Al₂O₃. *J Solid State Chem* 258:307–319. Doi:10.1016/j.jssc.2017.09.006

Figures

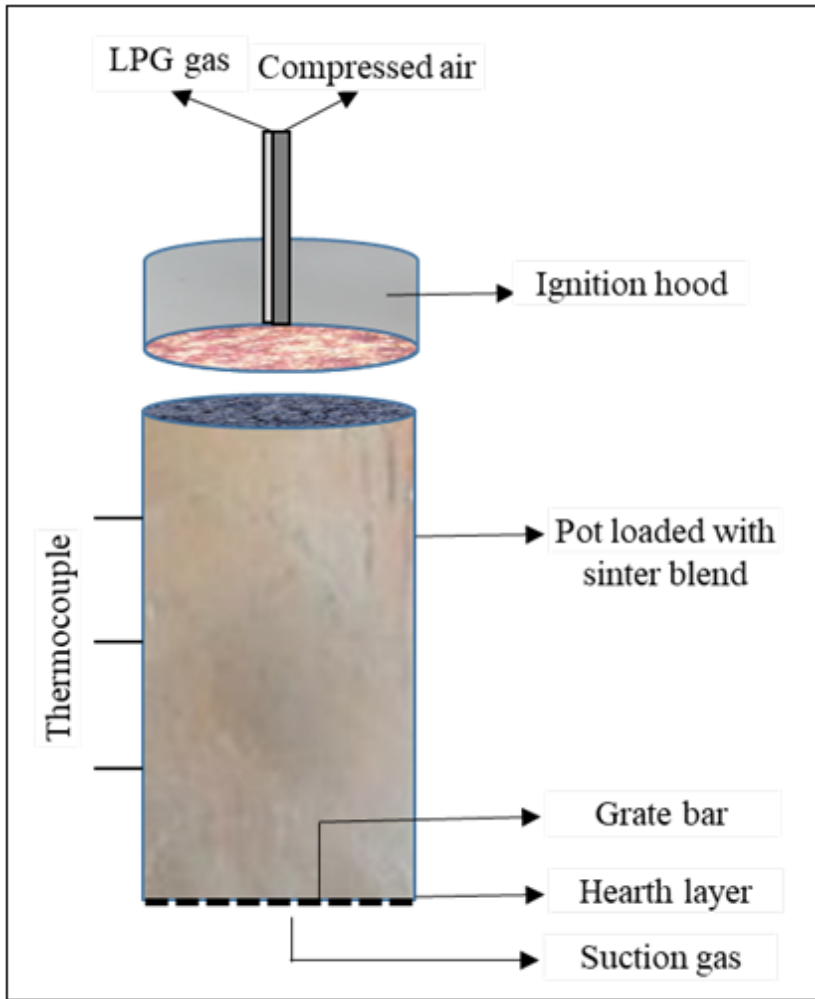


Figure 1

Laboratory sinter pot apparatus

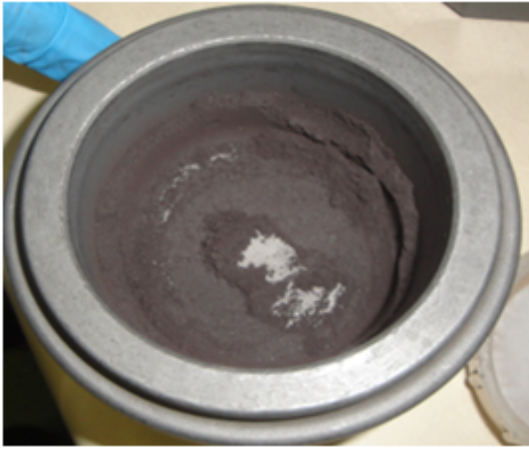


Figure 2

Preparation of the sintered sample for X-ray diffraction analysis.

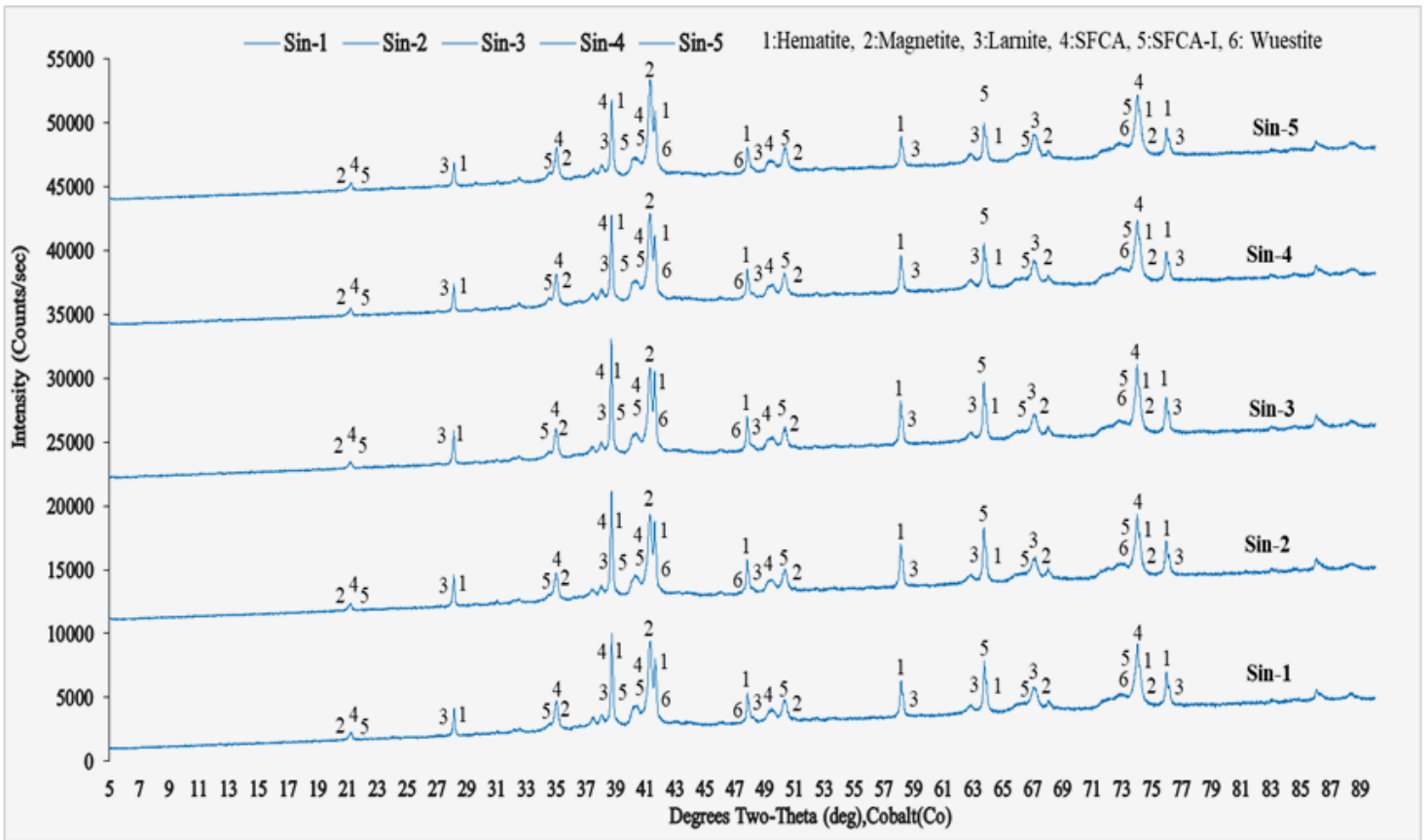


Figure 3

X-ray diffraction of sinter samples

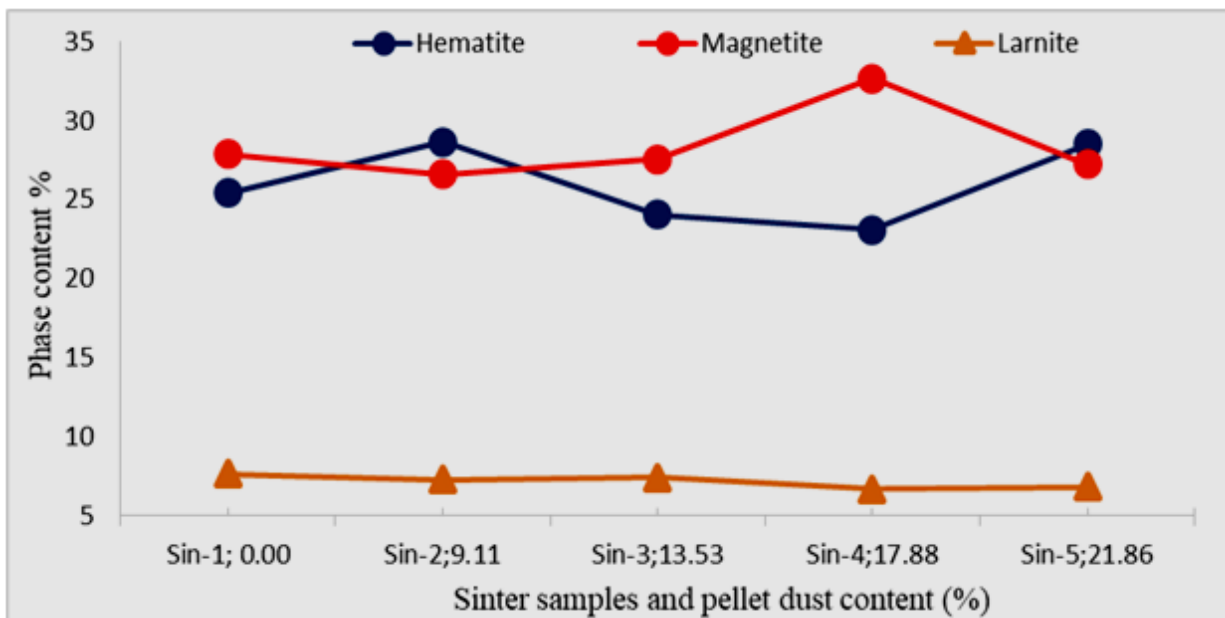


Figure 4

Change in hematite, magnetite, and larnite contents in the sinter after pellet dust use.

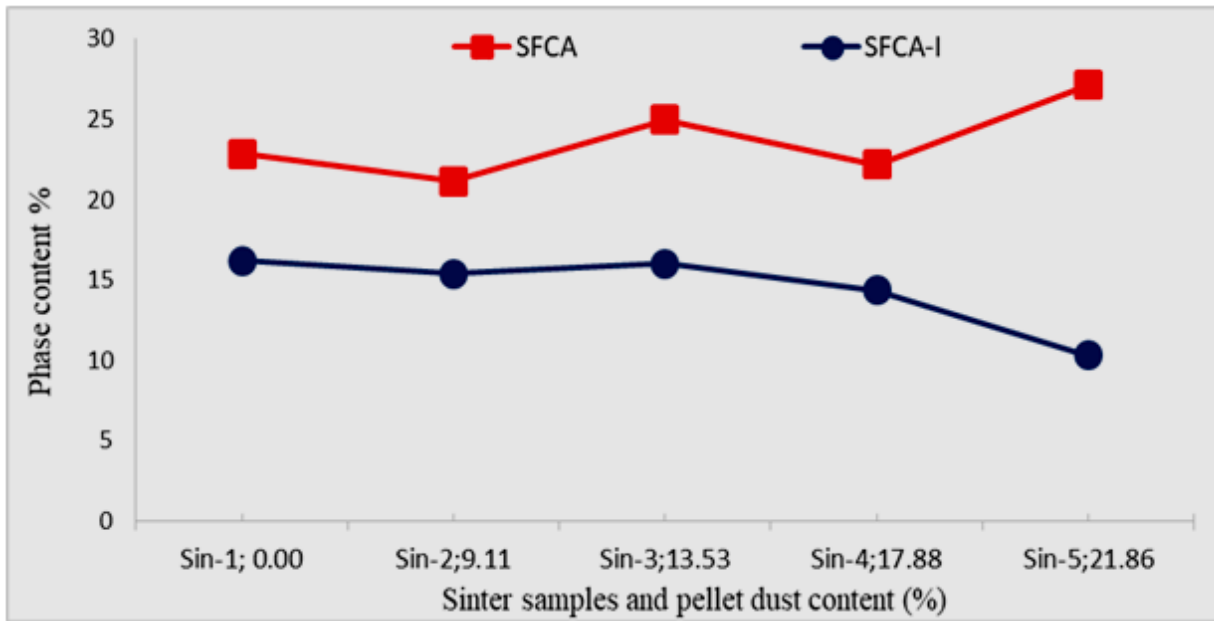


Figure 5

Change in SFCA and SFCA-I quantities after pellet dust use.

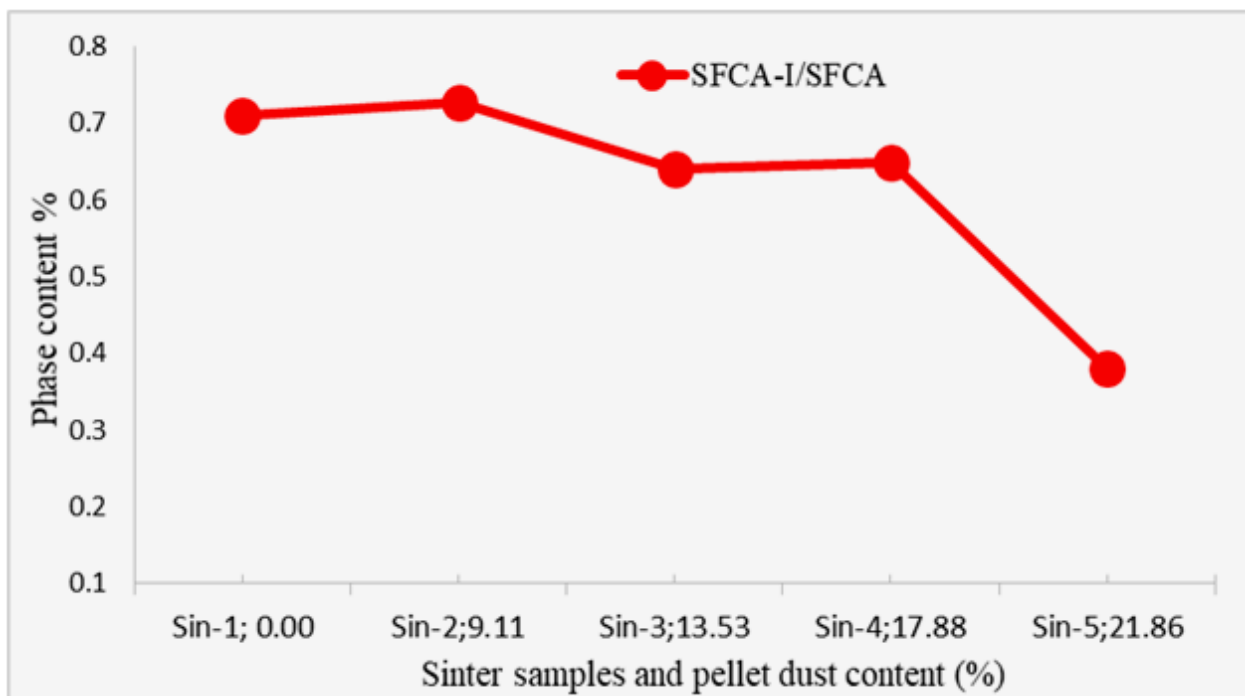


Figure 6

Change in SFCA-I/SFCA ratio of amount after pellet dust use.

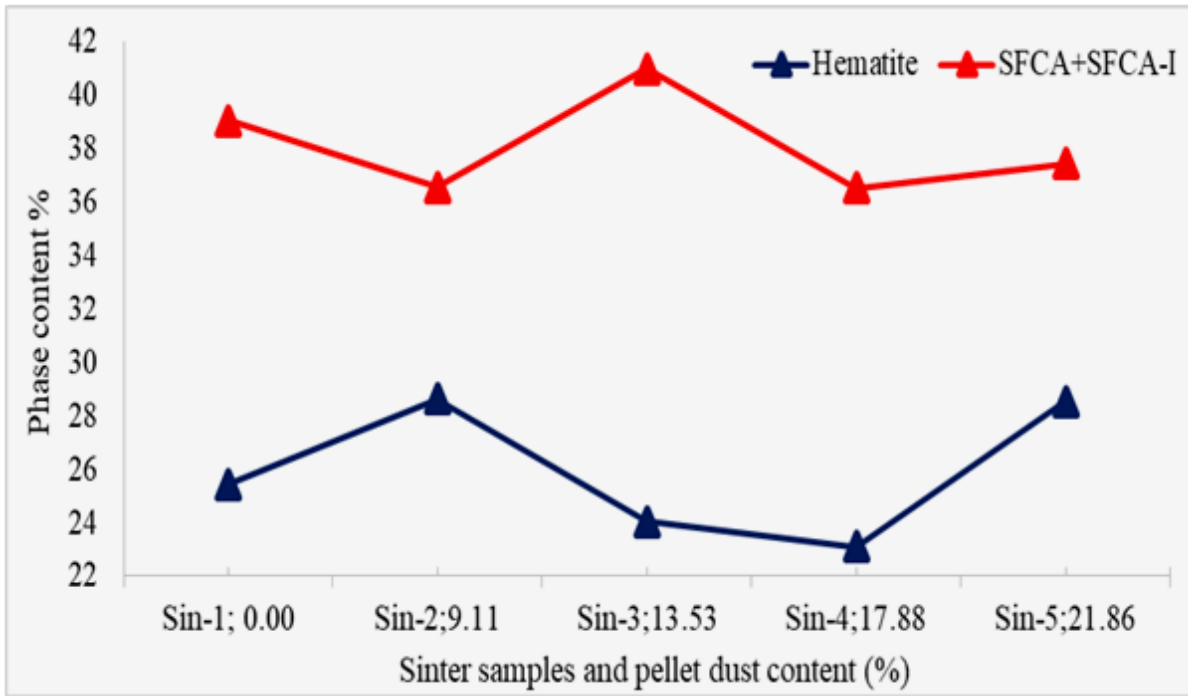


Figure 7

Variation of SFCA+SFCA-I and hematite phases in the sintered material.

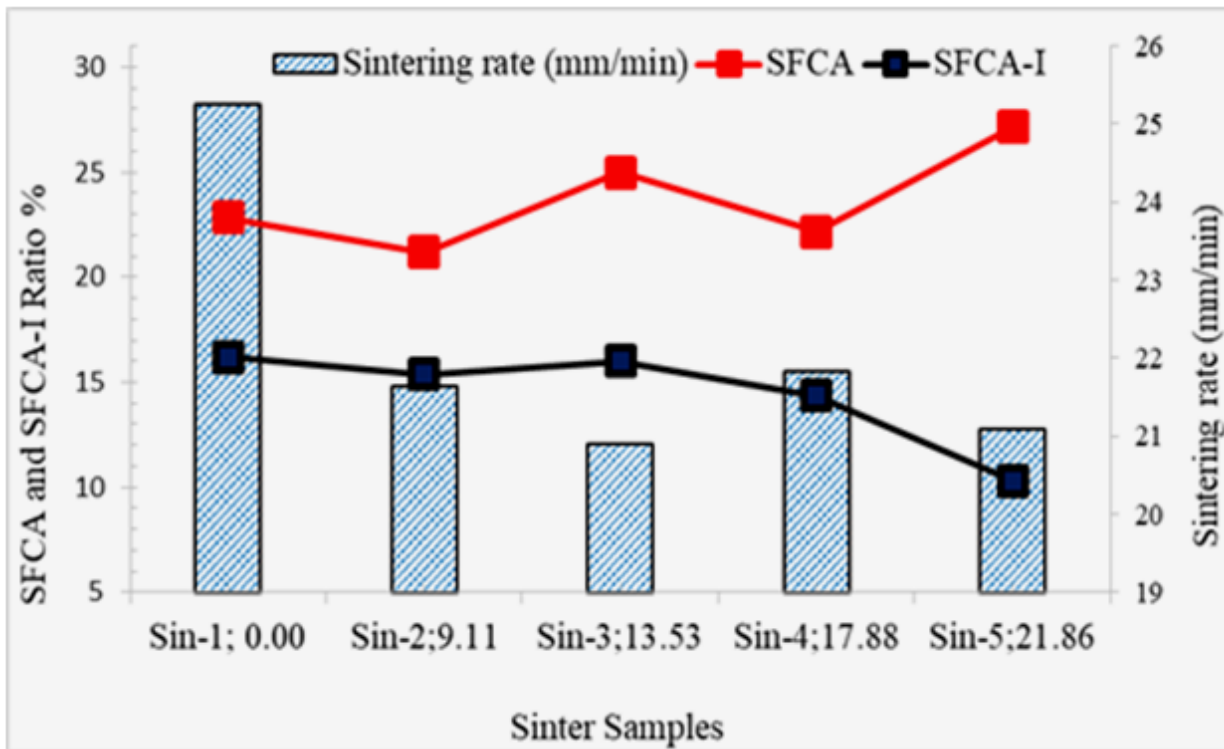


Figure 8

The effect of fine iron ore on the sintering rate, SFCA and SFCA-I.

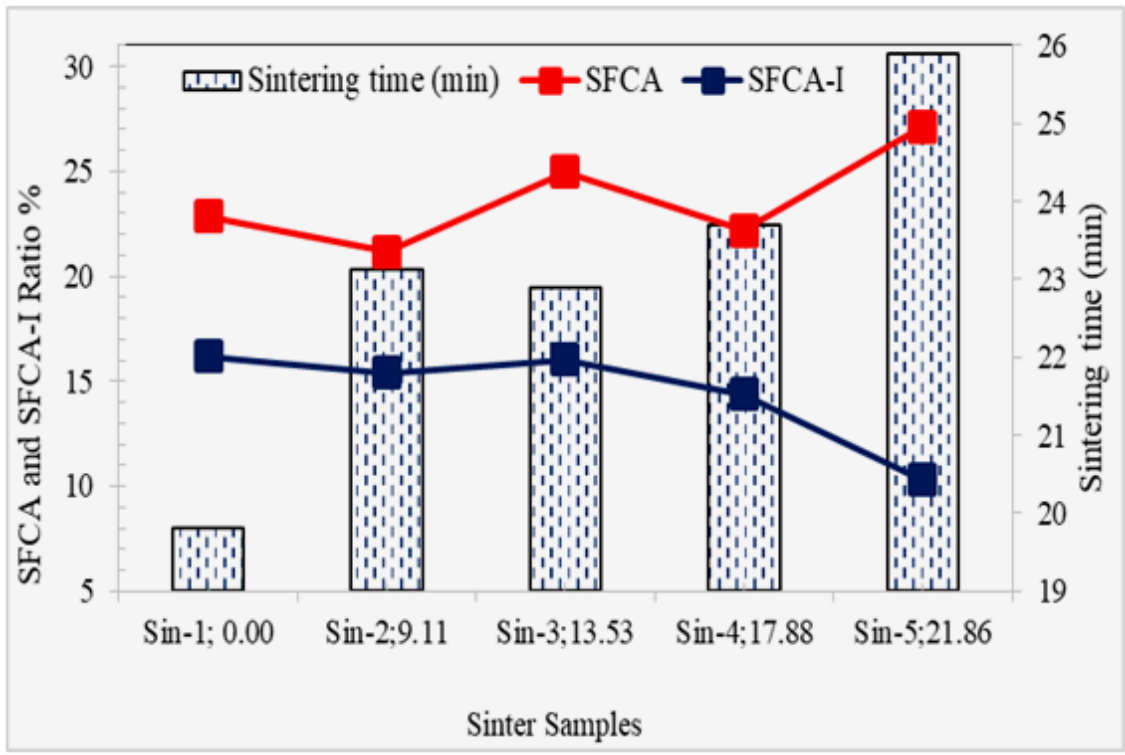


Figure 9

The effect of fine iron ore on the sintering time, SFCA and SFCA-I.

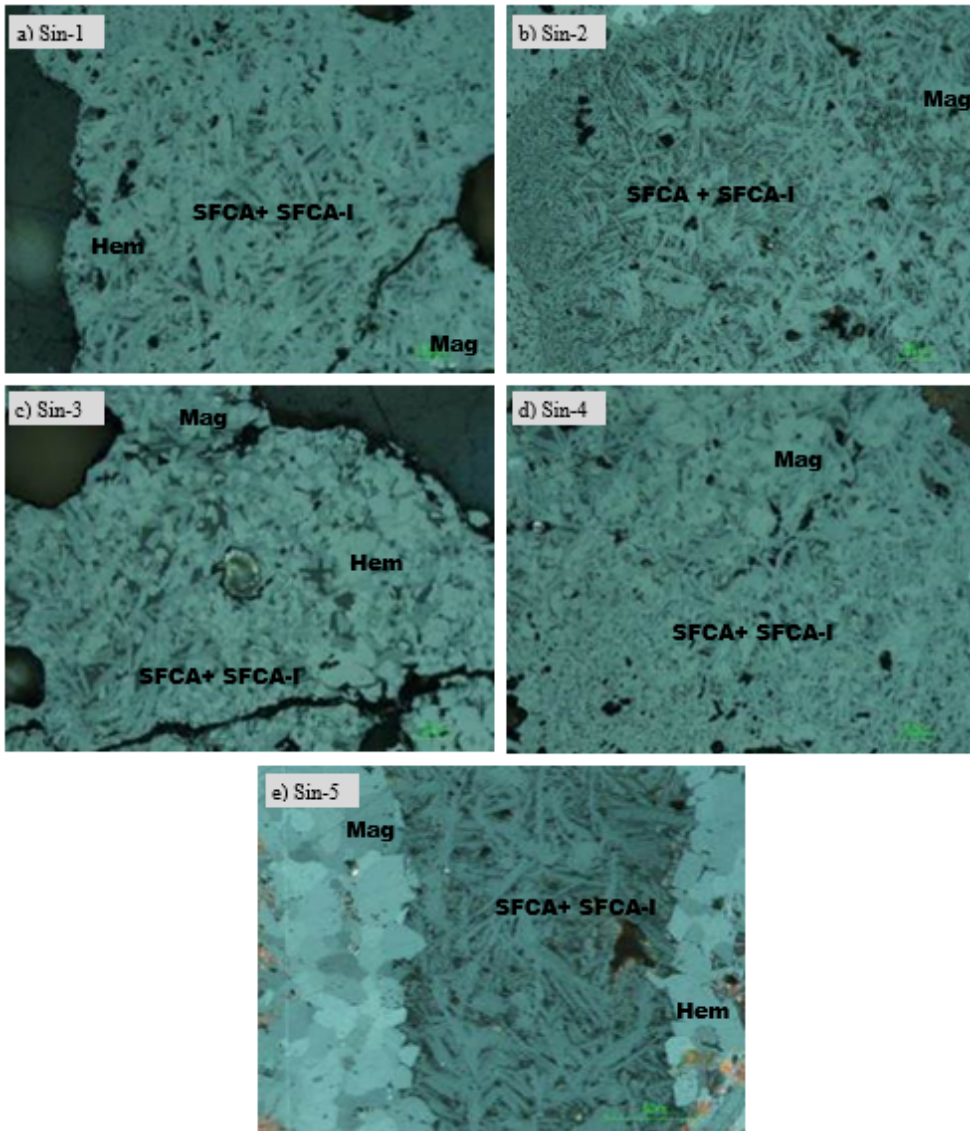


Figure 10

Optical micrograph of Sinter Samples. a) Sin-1, b) Sin-2, c) Sin-3, d) Sin-4, e) Sin-5, (Hem: Hematite, Mag: Magnetite, Silico Ferrite Calcium and Aluminum (SFCA), SFCA-I (X500)

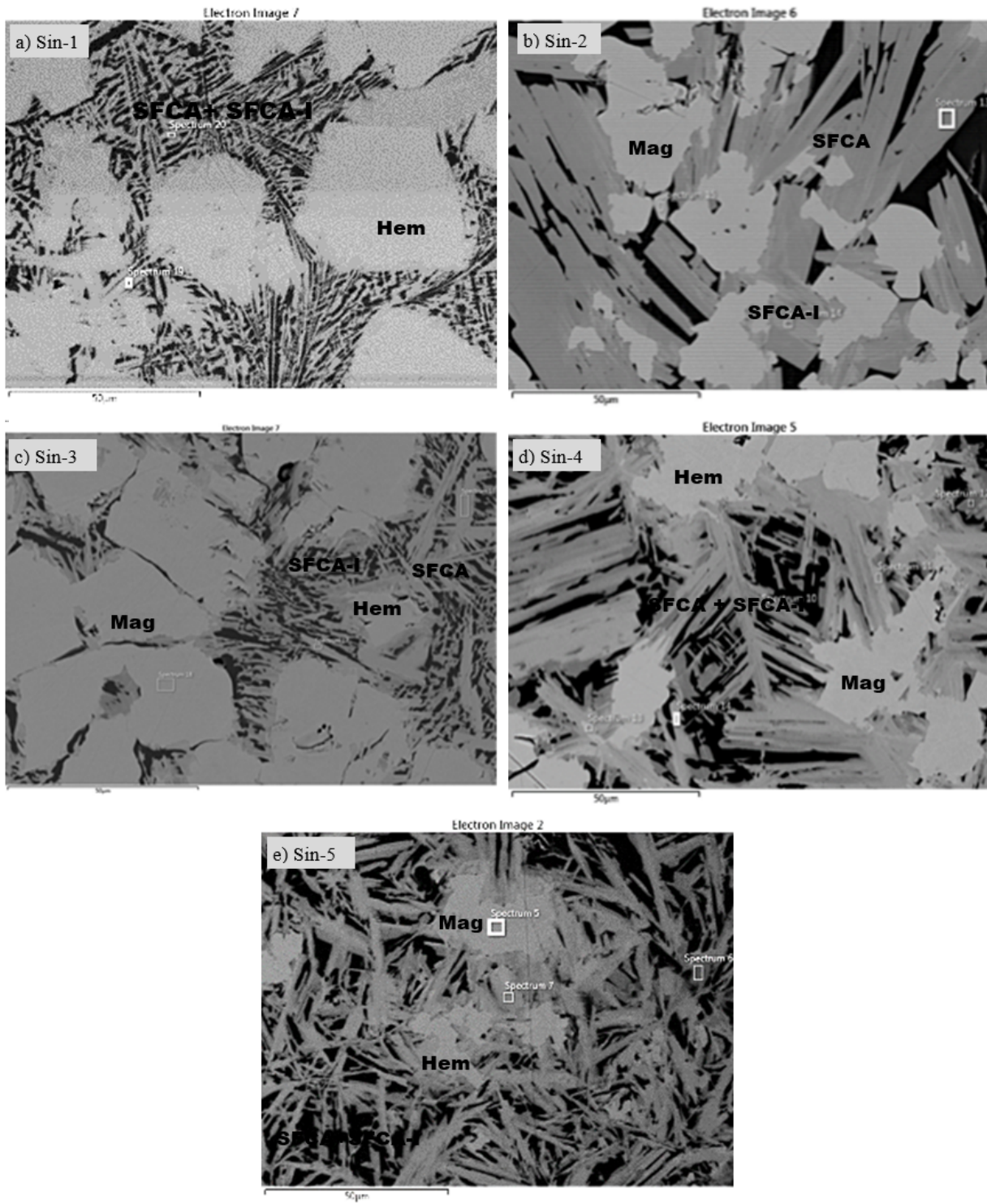


Figure 11

SEM micrographs of sintered bodies. a) Sin-1, b) Sin-2, c) Sin-3, d) Sin-4, e) Sin-5, (Hem: Hematite, Mag: Magnetite, Silico Ferrite Calcium and Aluminum (SFCA), SFCA- I (X1000)

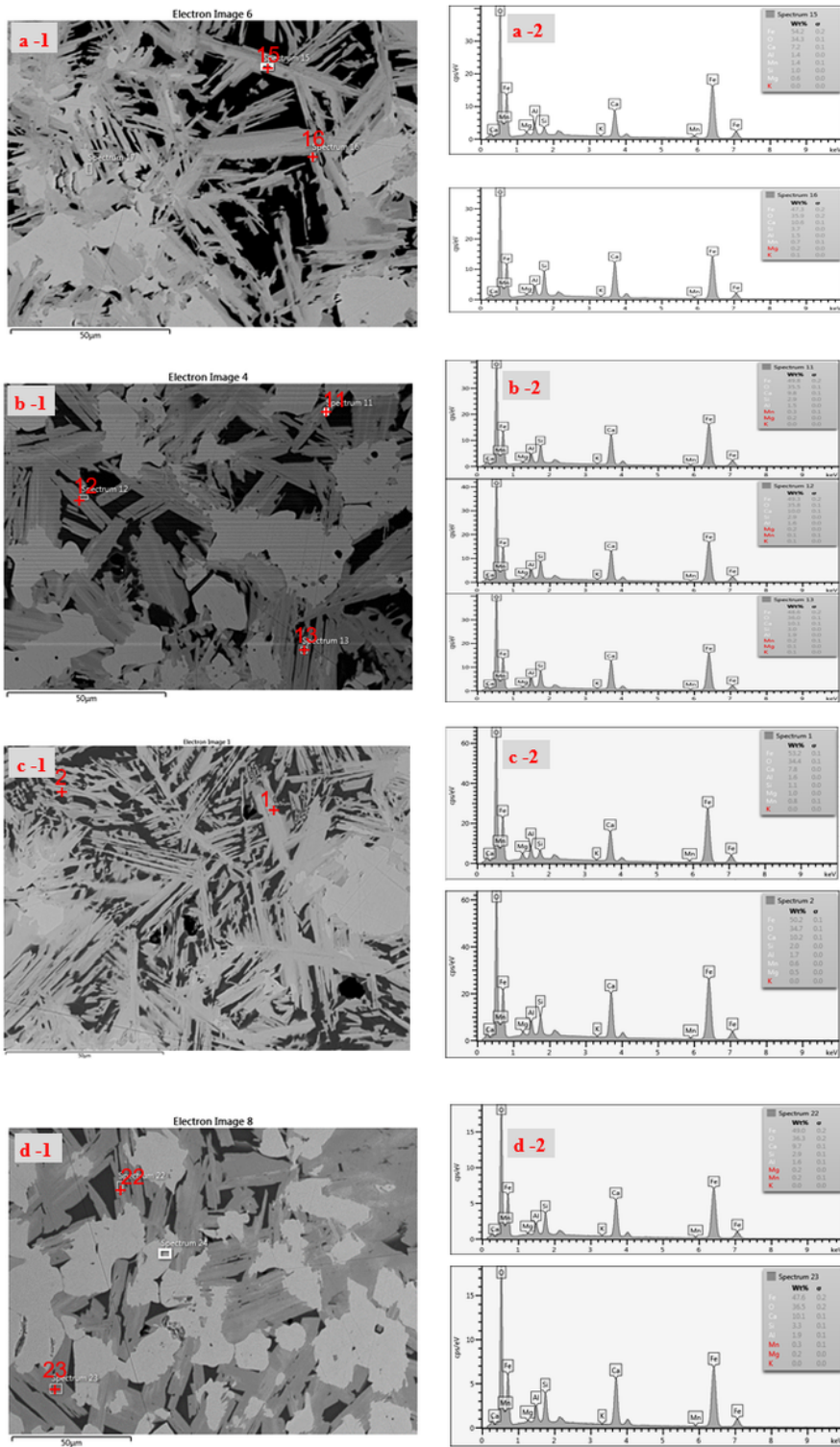


Figure 12

Structural morphology of SFCA. (a-1) SFCA and SFCA-I of SEM, (b-1) SFCA of SEM, (c-1) SFCA and SFCA-I of SEM, (d-1) SEM 's SFCA. (a-2) SFCA and SFCA-I of EDS, (b-2) SFCA of EDS, (c-2) SFCA and SFCA-I of EDS, (d-2) SFCA of EDS

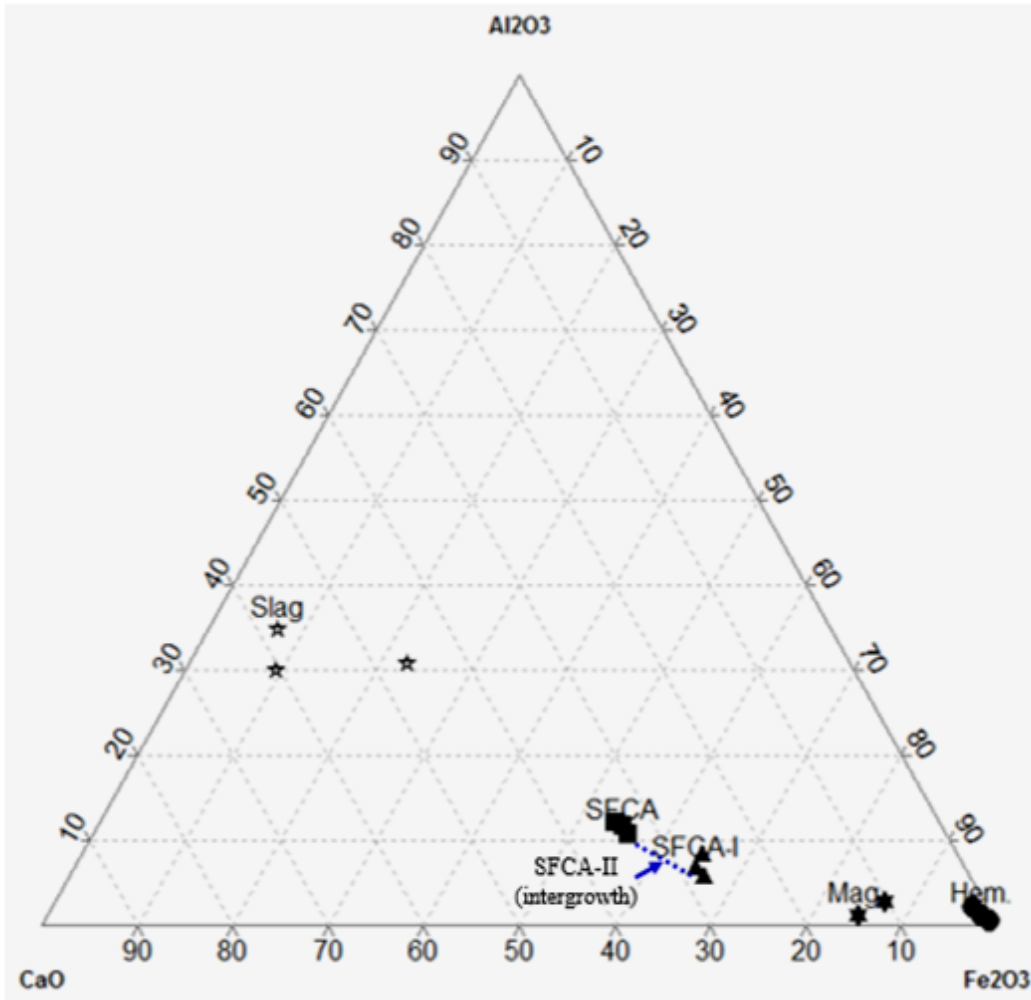


Figure 13

Schematic diagram of the compositional relationship between hematite, magnetite, SFCA and SFCA-I and SFCA-II in the sinter samples.

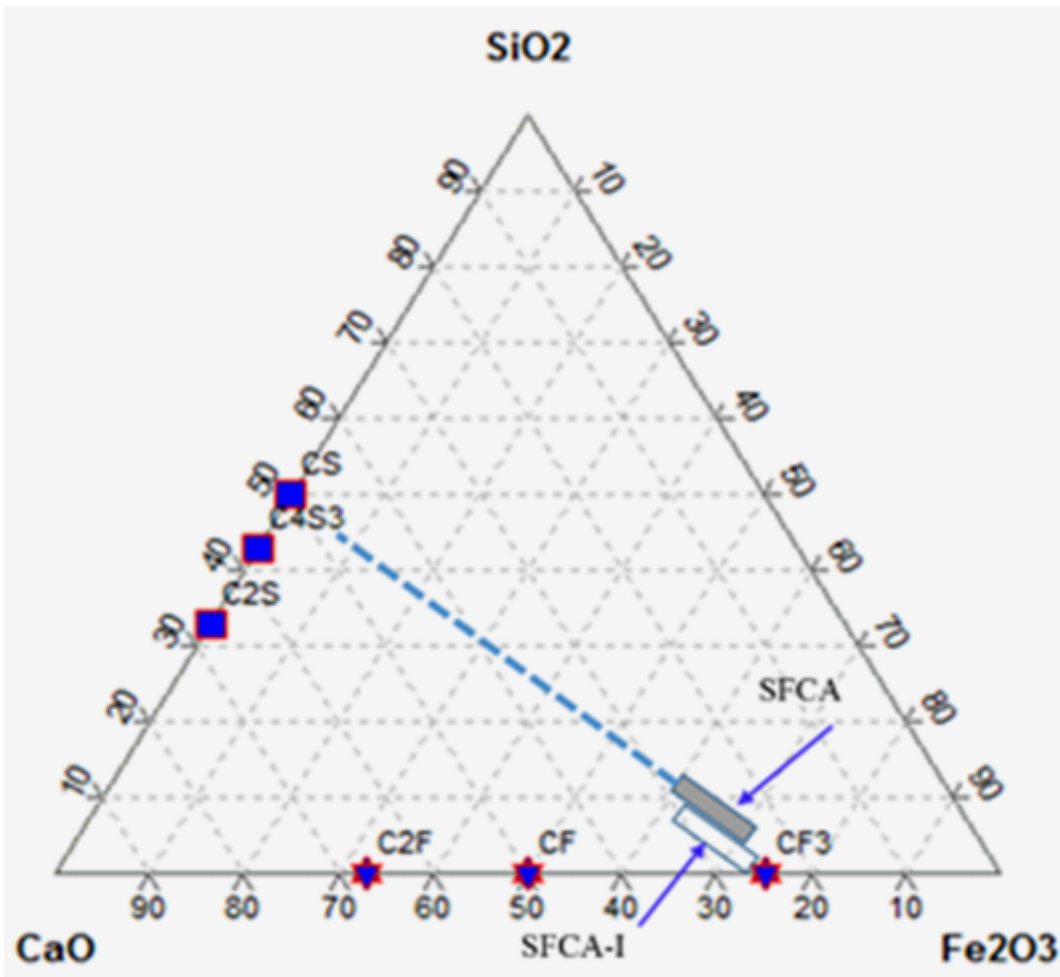


Figure 14

Schematic diagram of the compositional relationship between SFCA and SFCA-I within the Fe₂O₃-Al₂O₃-CaO-SiO₂.

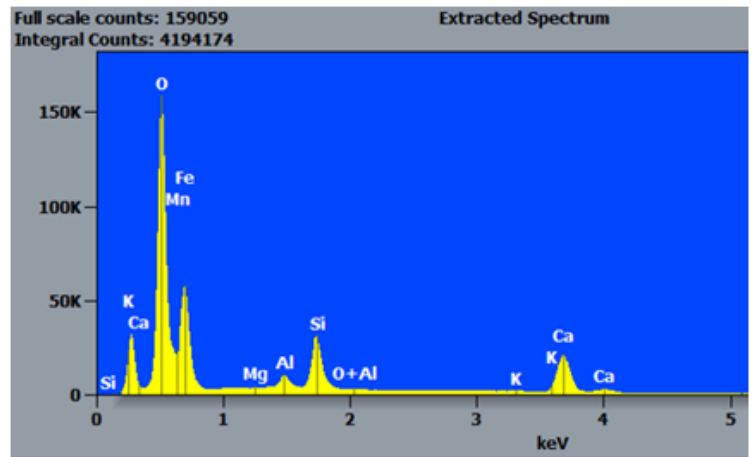
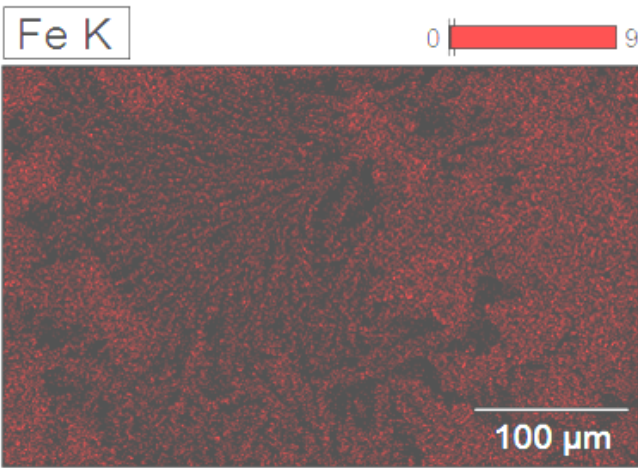
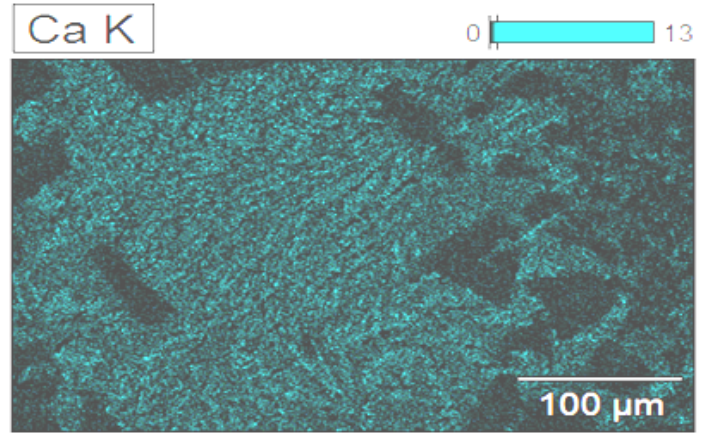
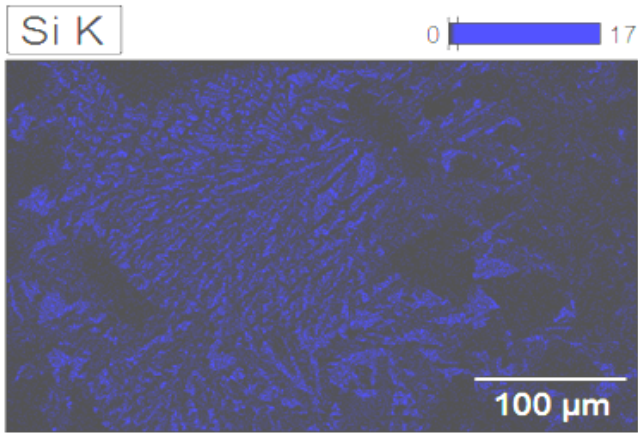


Figure 15

Element map (Si/Ca/Fe tri-element map, Scale bar in each image is 100 μm).

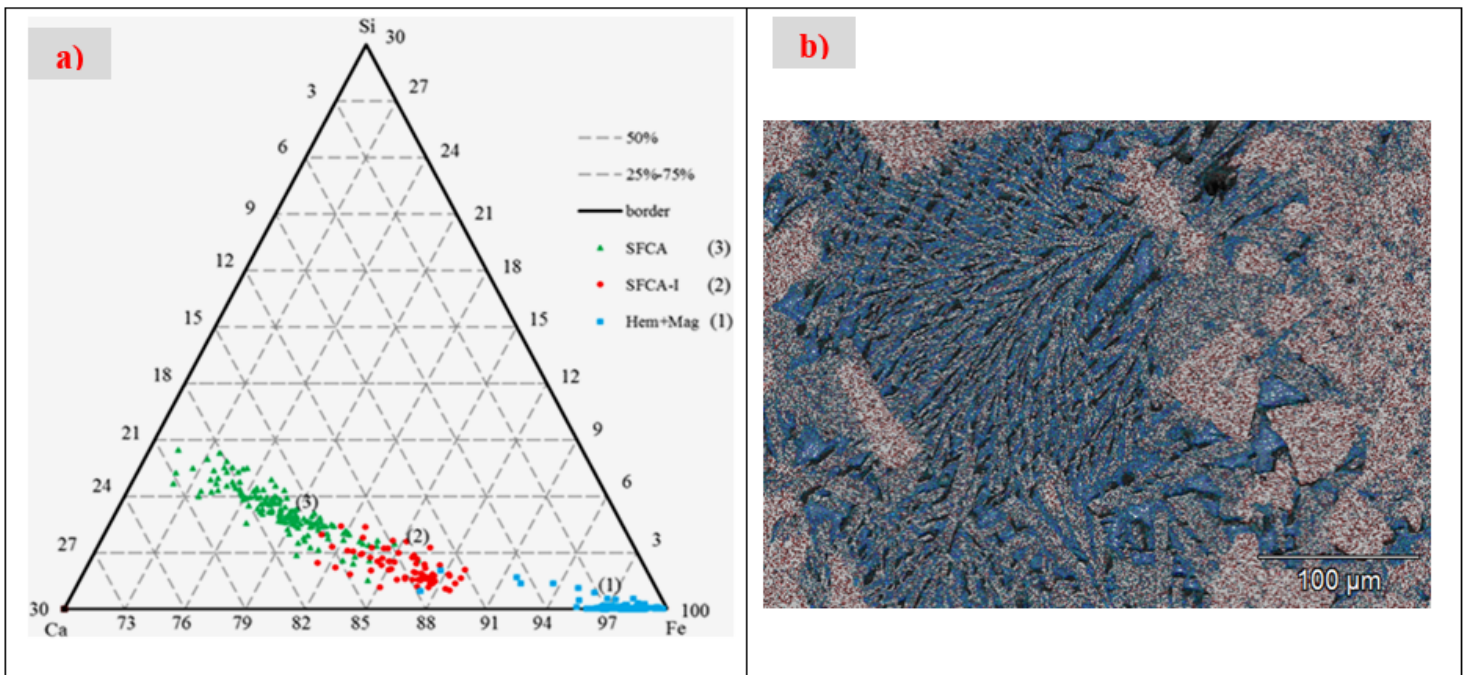


Figure 16

a) Microprobe analysis of the sinter samples. b) Mineral map of Si, Ca, and Fe (X1000)

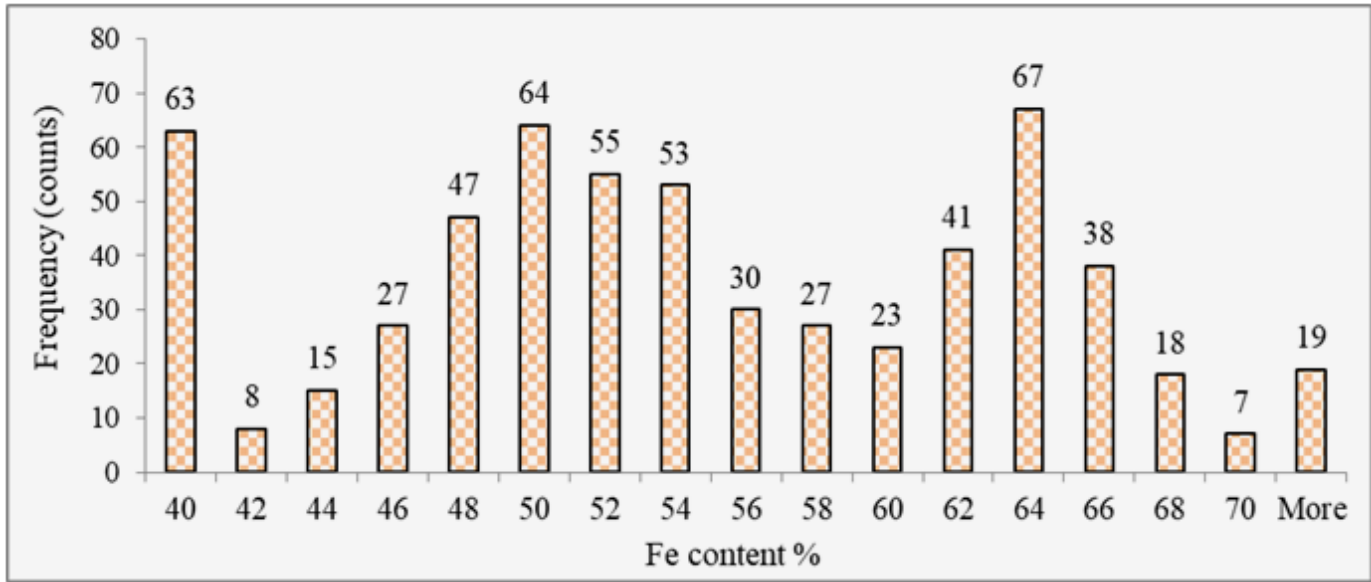


Figure 17

Change of Fe content (%) in the total sinter samples.

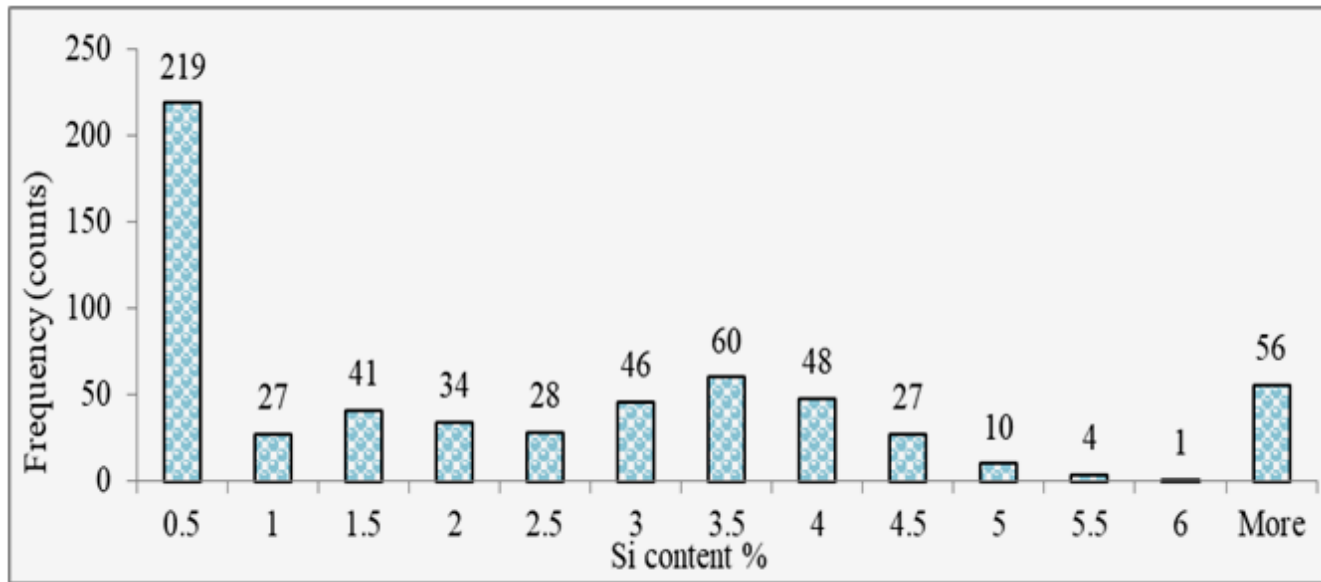


Figure 18

Change of Si content (%) in the total sinter samples.

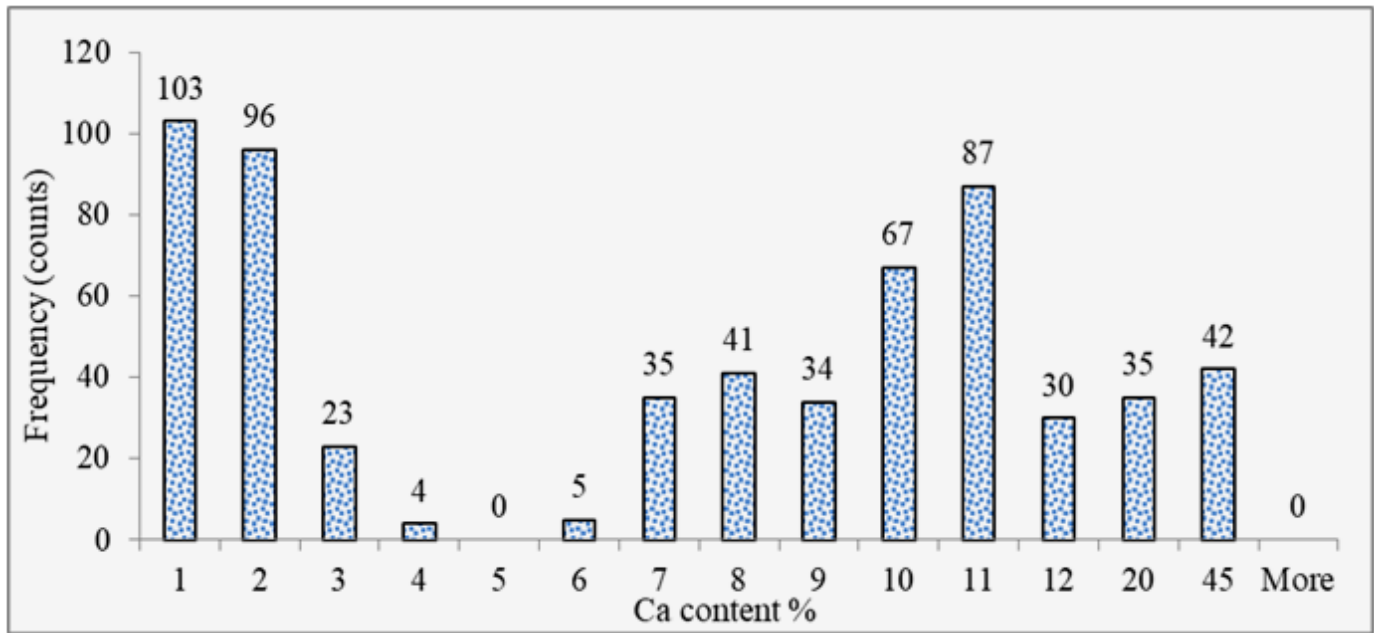


Figure 19

Change of Ca content (%) in the total sinter samples.

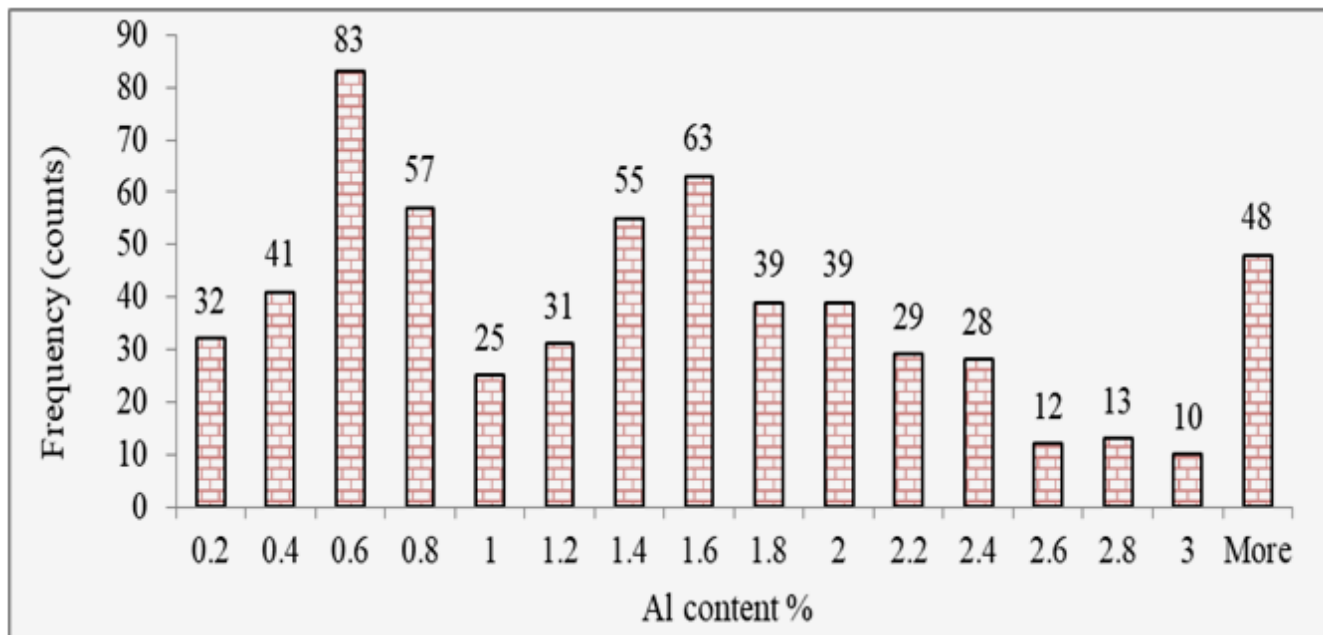


Figure 20

Change of Al content (%) in the total sinter samples.

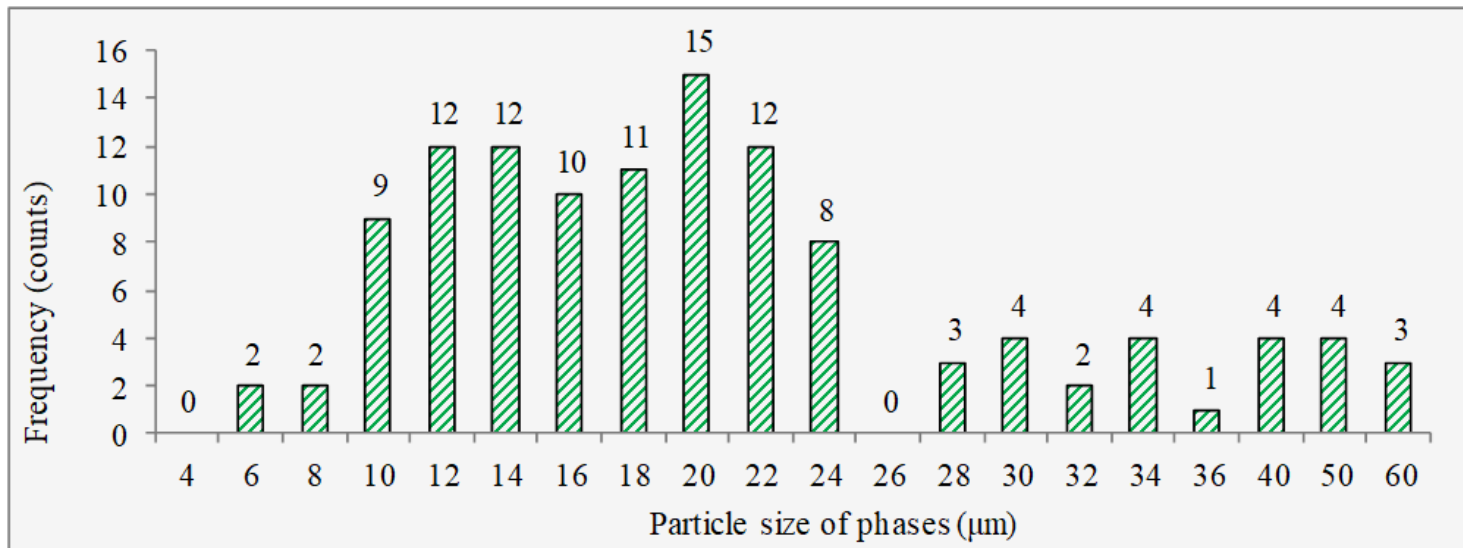


Figure 21

Crystal particle size distribution in total sinter samples

Supplementary Files

This is a list of supplementary files associated with this preprint. Click to download.

- [Highlight.S.BLKBAI.docx](#)